Gauge-Equivariant Graph Networks via Self-Interference Cancellation

Yoonhyuk Choi 1 Chong-Kwon Kim 2

Abstract

Graph Neural Networks (GNNs) excel on homophilous graphs but often fail under heterophily due to self-reinforcing and phase-inconsistent signals. We propose a Gauge-Equivariant Graph Network with Self-Interference Cancellation (GESC), which replaces additive aggregation with a projection-based interference mechanism. Unlike prior magnetic or gauge-equivariant GNNs that typically focus on phase handling in spectral filtering while largely relying on scalar weighting, GESC introduces a U(1) phase connection followed by a rank-1 projection that attenuates self-parallel components before attention. A sign- and phase-aware gate further regulates neighbor influence, attenuating components aligned with current node states and acting as a local notch on low-frequency modes. Across diverse graph benchmarks, our method consistently outperforms recent state-of-the-art models while offering a unified, interference-aware view of message passing. Our code is available at https://anonymous.4open.science/r/GESC-1B22.

1. Introduction

Graph Neural Networks (GNNs) have emerged as a powerful paradigm for learning on relational data, achieving state-of-the-art performance across social networks, recommendation, and scientific computing (Kipf & Welling, 2017; Veličković et al., 2018; Gilmer et al., 2017). Despite these successes, most GNNs rely on real-valued message passing that implicitly assumes homophily, symmetric interactions, and non-negative aggregation (Wu et al., 2019; Bronstein et al., 2021). This inductive bias aligns well with classical benchmarks but fails to represent the directional or oscillatory nature of many real-world systems.

Many graphs exhibit interfering interactions that cannot

Preprint

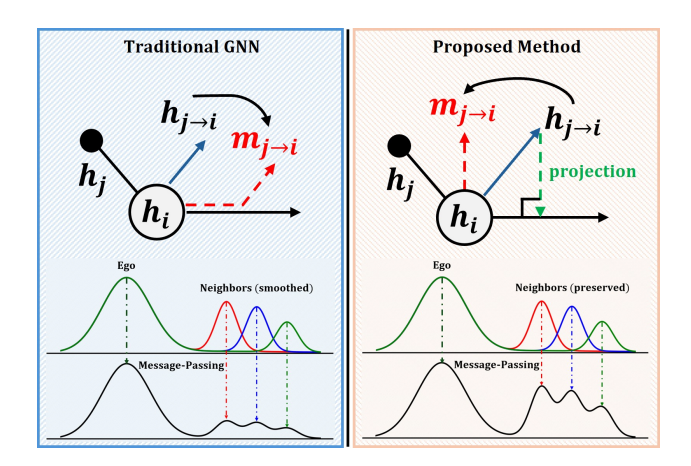


Figure 1: (*Left*) While traditional additive aggregation uniformly accumulates neighbor messages, (*right*) our wave-interference mechanism employs magnetic transport, SIC, and sign-aware gating to align phases and cancel redundant components, effectively suppressing detrimental neighbors while preserving informative signals.

be faithfully captured by additive aggregation. Such phenomena naturally arise in systems governed by transport, diffusion, or wave propagation, and can be modeled through magnetic Laplacians, signed-directed operators, or highfrequency spectral components (Levie et al., 2018; Rusch & Mishra, 2020; Marques et al., 2020; Wang et al., 2021; Lim et al., 2022; Ko et al., 2023). However, standard message passing aggregates neighbor signals indiscriminately, amplifying redundant components and suppressing antisymmetric structure. As illustrated in Figure 1 (left), repeated aggregation reinforces self-parallel messages over multiple hops, leading to constructive accumulation bias (so-called oversmoothing) (Li et al., 2018; Oono & Suzuki, 2019; Alon & Yahav, 2021; Black et al., 2023) and heterophily degradation (Zhu et al., 2020; Lim et al., 2021). This failure to represent destructive interference limits GNN expressivity in non-homophilous settings.

Recent studies have sought to alleviate these issues through more expressive aggregation using signed messaging (Huang et al., 2019; Li et al., 2022b; Choi et al., 2025a), heterophily-aware architectures (Jin et al., 2021; Choi et al., 2025b), adaptive or spectral filtering (Chien et al., 2021; He et al., 2021; Ma et al., 2021), or decomposition-based

¹Department of Artificial Intelligence, Sookmyung Women's University, Seoul, South Korea ²Department of Energy AI, Korea Institute of Energy Technology, Naju, South Korea. Correspondence to: Chong-Kwon Kim <ckim@kentech.ac.kr>.

designs (Wang & Derr, 2021; Yan et al., 2022). While these models mitigate over-smoothing, they remain fundamentally scalar reweighting schemes that fail to represent the phase structure of interactions. Without explicit modeling of relative phases or destructive alignment, such approaches cannot express oscillatory or signed behaviors essential for directional and anti-homophilous graphs (Levie et al., 2018; Xu et al., 2019; de Haan et al., 2021; Brandstetter et al., 2022; Zheng et al., 2022; Rampášek et al., 2022). This motivates a principled mechanism that directly models and cancels interference, rather than merely reweighting it away.

To realize this idea, our model represents nodes as complex embeddings and equips each edge with a learnable U(1)phase connection with gauge-equivariant transport (de Haan et al., 2021; Brandstetter et al., 2022). Unlike prior magnetic Laplacian-based or gauge-equivariant GNNs (Zhang et al., 2021; He et al., 2022), which primarily achieve phaseconsistent message passing through scalar reweighting, we introduce a projection-based self-interference cancellation that enables true gauge- and permutation-equivariant filtering within the complex message space. As illustrated in Figure 1 (right), our interference-aware design removes redundant components at their source and aligns neighbor messages through magnetic transport and sign-aware gating. Specifically, (i) a projection-based Self-Interference Cancellation (SIC) removes redundant components before attention; (ii) a sign-aware gate modulates neighbors based on their relative phase; and (iii) an interference-aware message passing achieves stable propagation and mitigates oversmoothing at finite depth. Our contributions are threefold:

- We introduce Self-Interference Cancellation (SIC), a projection-based mechanism that removes redundant self-aligned components, mitigating constructive accumulation bias and reducing over-smoothing in GNNs.
- We propose a Sign-aware Gating with Gauge Transport mechanism that leverages complex phase alignment for smooth and stable modulation without relying on explicit direction labels.
- We provide theoretical analysis and extensive empirical evaluation on synthetic and real-world graph benchmarks, demonstrating improved stability, heterophily robustness, and state-of-the-art performance.

2. Related Work

Graph Neural Networks and Heterophily. Classical GNNs are highly effective in homophilous regimes, but degrade significantly on heterophilous graphs (Defferrard et al., 2016; Kipf & Welling, 2017; Veličković et al., 2018; Gilmer et al., 2017; Abu-El-Haija et al., 2019). To address this, a large body of work introduces signed or adaptive

propagation mechanisms (Derr et al., 2018; Klicpera et al., 2019; Gasteiger et al., 2019; Huang et al., 2019; Bo et al., 2021; Chien et al., 2021; Du et al., 2022; Choi et al., 2025a). Recent studies also propose link-level features (Lim et al., 2021) and decomposition-based heterophily models (Wang & Derr, 2021; Yan et al., 2022). Unlike these approaches, our formulation targets heterophily through geometric interference control rather than edge reweighting, explicitly cancelling redundant self-components via rank-1 projection before attention and applying sign-aware gating.

Complex and Spectral-Phase Representations. A second line of work leverages complex embeddings to encode antisymmetry (Trouillon et al., 2016; Sun et al., 2019). Early spectral (Levie et al., 2018) and more recent graph networks (Zhang et al., 2019; 2022) demonstrate that complex-valued filtering can naturally encode phase and orientation. Magnetic Laplacian formulations introduce complex Hermitian operators (Zhang et al., 2021; He et al., 2022), and recent spectral designs extend this idea to richer frequency responses (Rusch & Mishra, 2020). Most prior works incorporate phase information only at the filtering level or as an auxiliary feature. In contrast, we inject phase alignment directly into spatial attention and gating and guarantee gauge-invariant scoring within message passing.

Gauge Equivariance and Phase Transport. Building on these phase-based designs, gauge-equivariant networks formalize invariance to local reference frames (Cohen & Welling, 2016; Cohen et al., 2019; de Haan et al., 2021), with recent developments connecting geometric deep learning to physical principles (Pei et al., 2020; Bronstein et al., 2021; Brandstetter et al., 2022; Luo et al., 2022). We reinterpret edge phases as latent directional transport to ensure scalar scores and alignments remain gauge-invariant within our gating mechanism. This treatment complements magnetic and spectral designs (Marques et al., 2020; Zhang et al., 2021; He et al., 2022; Lim et al., 2022), but differs by learning phase transport end-to-end in the spatial domain.

Over-smoothing and Interference. Deep message passing often causes representation homogenization (Li et al., 2018; Oono & Suzuki, 2019; Alon & Yahav, 2021; Black et al., 2023), limiting expressivity. Typical fixes include residual connections, normalization, or hop-wise feature mixing (Klicpera et al., 2019; Gasteiger et al., 2019; Frasca et al., 2020; Wang et al., 2021). Our Self-Interference Cancellation (SIC) module takes a geometric approach: it projects out the transported neighbor component parallel to the target state before attention, mitigating self-reinforcement and preserving orthogonal signals. This stands in contrast to heuristic ego—neighbor separation methods such as H₂GCN (Zhu et al., 2020), offering a principled interference control mechanism tied to phase alignment.

3. Preliminaries

Graph structure. Let $\mathcal{G}=(\mathcal{V},\mathcal{E},X)$ denote a finite undirected attributed graph, to establish notation for subsequent sections. The node feature matrix $X\in\mathbb{R}^{N\times d_{\mathrm{in}}}$ encodes d_{in} -dimensional real-valued features for each node. The topology is represented by a symmetric adjacency matrix $A\in\{0,1\}^{N\times N}$ with $A_{ij}=A_{ji}=1$ if and only if $\{i,j\}\in\mathcal{E}$. We denote by D the diagonal degree matrix $D_{ii}=\sum_{j=1}^N A_{ij}$ and by $\mathcal{N}(i)$ the neighbor set of node i. Each node i has a label $y_i\in\{1,\ldots,C\}$, and $Y\in\mathbb{R}^{N\times C}$ is the one-hot label matrix. Following Zhu et al. (2020), the global homophily level is given by:

$$\mathcal{G}_h := \frac{1}{|\mathcal{E}|} \sum_{\{i,j\} \in \mathcal{E}} \mathbb{I}(y_i = y_j), \tag{1}$$

where lower \mathcal{G}_h indicates stronger heterophily. We focus on semi-supervised node classification with a labeled subset \mathcal{V}_L and unlabeled nodes $\mathcal{V}_U = \mathcal{V} \setminus \mathcal{V}_L$.

Complex node embeddings and notation. We operate in a complex vector space \mathbb{C}^d , which naturally encodes both magnitude and phase information. Each node i carries an embedding $h_i^{(t)} \in \mathbb{C}^d$ at layer t, and the entire node representation is as follows:

$$H^{(t)} = \begin{bmatrix} (h_1^{(t)})^\top \\ \vdots \\ (h_N^{(t)})^\top \end{bmatrix} \in \mathbb{C}^{N \times d}. \tag{2}$$

The initial embedding is obtained by linearly mapping real-valued features into the complex domain using two real weight matrices for the real and imaginary parts. We denote the conjugate transpose by $(\cdot)^H$, the elementwise complex conjugate by $\overline{(\cdot)}$, $\tilde{\cdot}$ (tilde) for transported quantities, and $\hat{\cdot}$ (hat) for post-gating messages.

Complex inner products and projections. For $u, v \in \mathbb{C}^d$, the complex inner product is defined as

$$\langle u, v \rangle_{\mathbb{C}} = u^{\mathrm{H}}v = \sum_{k=1}^{d} \overline{u_k} v_k, \quad \|u\|_2 = \sqrt{\langle u, u \rangle_{\mathbb{C}}}.$$
 (3)

We use a Tikhonov-regularized rank-1 projector $\Pi_{\epsilon}(h_i)$ onto the (one-dimensional) subspace spanned by h_i to separate the self-parallel and orthogonal components of messages:

$$\Pi_{\epsilon}(h_i) = \frac{h_i h_i^{\mathrm{H}}}{\|h_i\|_2^2 + \epsilon},\tag{4}$$

with $\epsilon > 0$ for numerical stability. This operator will play a central role in the self-interference cancellation (SIC) mechanism introduced in Section 4.

Edge transport and phase structure. Each undirected edge $\{i, j\}$ is assigned a unit-magnitude complex phase factor $\theta_{ji} \in \mathbb{R}$, which induces a directed pair of parallel transports with opposite phases:

$$U_{ji} := e^{i\theta_{ji}}, \quad U_{ij} := \overline{U_{ji}} = e^{-i\theta_{ji}},$$
 (5)

where $|U_{ji}| = |U_{ij}| = 1$. We use complex weights $W, Q \in \mathbb{C}^{d \times d}$ (indices omitted here for clarity). The transported source in *i*'s reference frame is then given by

$$\tilde{h}_{i \to i} = U_{ii} W h_i. \tag{6}$$

Gauge-invariant formulation. For arbitrary phases $\{\psi_i\}$, we adopt a local U(1) gauge symmetry:

$$h_i \mapsto e^{i\psi_i} h_i,$$
 (7)

$$(\theta_{ji}, U_{ji} = e^{i\theta_{ji}}) \mapsto (\theta_{ji} + \psi_i - \psi_j, e^{i(\psi_i - \psi_j)}U_{ji}).$$

Then, $\tilde{h}_{j\to i}\mapsto \tilde{h}'_{j\to i}=e^{i\psi_i}\tilde{h}_{j\to i}$ (gauge-equivariant). If W,Q are gauge-invariant linear maps, scalar alignments like

$$\left(Qh_i\right)^{\mathrm{H}}\tilde{h}_{j\to i}\tag{8}$$

are exactly gauge-invariant, because both factors acquire the same local phase $e^{i\psi_i}$ which cancels out in the Hermitian product. This invariance ensures that all subsequent attention logits and projection scores in Section 4 are computed within a locally gauge-consistent reference frame.

4. Method

4.1. Overview

We replace additive neighbor accumulation in GNNs with a wave-interference mechanism that (i) cancels redundant self-components before attention, (ii) softly modulates neighbor messages with a sign-aware gate to reduce harmful influence without over-suppressing negative correlations, and (iii) leverages complex-valued representations with magnitude-robust nonlinearities and optional phase-aware attention. To further stabilize sign-aware gating under noisy neighbors, we employ a magnetic transport $U_{ji}=e^{i\theta_{ji}}$ (Section 3), which ensures gauge-invariant alignment and improves robustness in practice. All operations follow the gauge transformation convention, preserving gauge invariance of scalar scores and alignment terms.

4.2. Proposed Method

SIC and Complex Scoring. Each layer uses M heads. Head m applies a source transport $W^{(m)} \in \mathbb{C}^{d \times d}$ and a target filter $Q^{(m)} \in \mathbb{C}^{d \times d}$. For each neighbor $j \in \mathcal{N}(i)$ (induced direction $j \to i$), we use the unit-modulus transport defined in Section 3:

$$U_{ji} = e^{i\theta_{ji}}, \quad U_{ij} = \overline{U_{ji}}.$$
 (9)

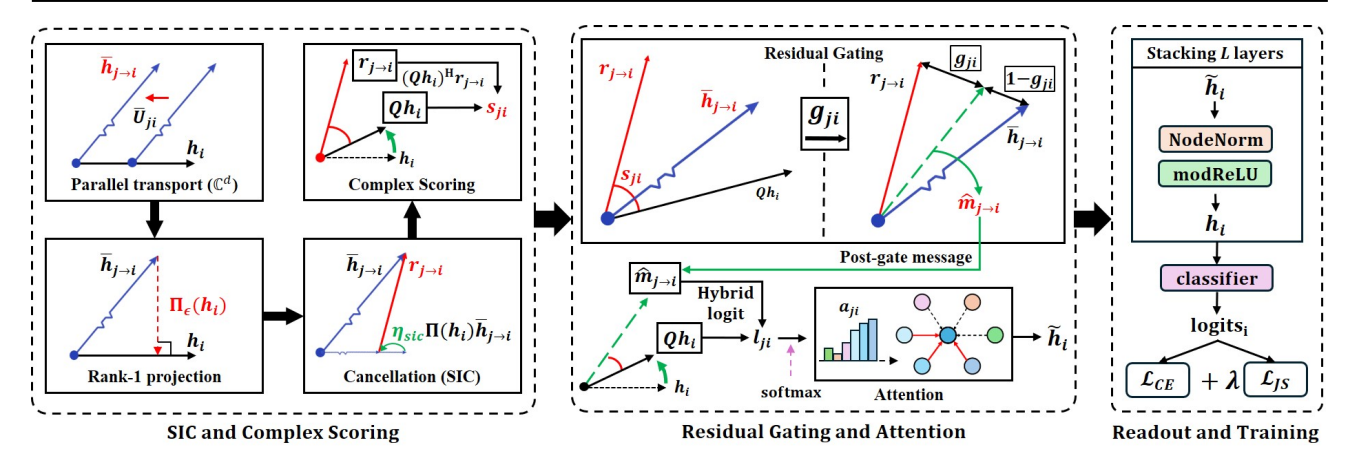


Figure 2: Overview of GESC. (*Left*) Neighbor messages are parallel transported and self-parallel components are cancelled via rank-1 projection, yielding gauge-invariant complex scores. (*Middle*) A sign-aware residual gate softly interpolates messages before hybrid magnitude-phase attention. (*Right*) Aggregated features undergo NodeNorm and modReLU, followed by classification with cross-entropy and JS consistency.

The transported source feature in i's reference frame is

$$\tilde{h}_{j \to i}^{(m)} \coloneqq U_{ji} W^{(m)} h_j^{(t)} \in \mathbb{C}^d. \tag{10}$$

To remove redundant self-parallel components before attention, we apply a Tikhonov-regularized rank-1 projector onto the target state $h_i^{(t)}$:

$$\Pi_{\epsilon}(h_{i}^{(t)}) \coloneqq \frac{h_{i}^{(t)}(h_{i}^{(t)})^{\mathrm{H}}}{\|h_{i}^{(t)}\|_{2}^{2} + \epsilon},$$

$$r_{j \to i}^{(m)} \coloneqq \tilde{h}_{j \to i}^{(m)} - \eta_{\mathrm{sic}} \cdot \Pi_{\epsilon}(h_{i}^{(t)}) \tilde{h}_{j \to i}^{(m)},$$
(11)

where $\eta_{\rm sic} \in [0, 1]$ controls cancellation strength and $\epsilon > 0$ ensures numerical stability. The complex alignment score is

$$s_{ii}^{(m)} := (Q^{(m)} h_i^{(t)})^{\mathsf{H}} r_{i \to i}^{(m)} \in \mathbb{C}.$$
 (12)

By the U(1) gauge convention (Section 3), $s_{ji}^{(m)}$ is a gauge-invariant scalar. For brevity, we denote the magnitude product used for normalized real alignment in the gate as

$$\nu_{ji}^{(m)} := \|Q^{(m)}h_i^{(t)}\|_2 \|r_{j\to i}^{(m)}\|_2 + \epsilon. \tag{13}$$

Sign-aware (phase-consistent) gating. We modulate the SIC-residual $r_{j \to i}^{(m)}$ by a sign-aware scalar gate $\xi_{ji}^{(m)} \in [0,1]$ computed from a gauge-invariant alignment:

$$\rho_{ji}^{(m)} := \operatorname{Re}\left(\frac{s_{ji}^{(m)}}{\nu_{ji}^{(m)}}\right),$$

$$\xi_{ji}^{(m)} := \sigma(c_m \rho_{ji}^{(m)} + d_m),$$
(14)

where c_m, d_m are learnable scalars and $\sigma(x) = \frac{1}{1+e^{-x}}$. The sign-aware residual is

$$\bar{r}_{j \to i}^{(m)} \coloneqq \xi_{ji}^{(m)} r_{j \to i}^{(m)}.$$
 (15)

Residual Gating and Alignment-based Attention. Each head learns a residual mixing gate $g_{ii}^{(m)} \in [0,1]$:

$$g_{ji}^{(m)} = \sigma \left(a_m^{\top} \left[\varphi(\|\bar{r}_{j \to i}^{(m)}\|_2), \varphi(\|\tilde{h}_{j \to i}^{(m)}\|_2), \varphi(|s_{ji}^{(m)}|) \right] + b_m \right), \tag{16}$$

where $\varphi(x) = \log(1+x)$. The post-gate message is

$$\widehat{m}_{j \to i}^{(m)} := g_{ji}^{(m)} \bar{r}_{j \to i}^{(m)} + \left(1 - g_{ji}^{(m)}\right) \tilde{h}_{j \to i}^{(m)}. \tag{17}$$

Attention logits are computed from the complex alignment between the target and post-gate message:

$$\tilde{s}_{ii}^{(m)} := (Q^{(m)} h_i^{(t)})^{\mathrm{H}} \hat{m}_{i \to i}^{(m)}. \tag{18}$$

For the attention normalization, we use a separate magnitude product with a hybrid logit that combines magnitude and normalized real alignment:

$$\tilde{\nu}_{ji}^{(m)} := \|Q^{(m)} h_i^{(t)}\|_2 \|\widehat{m}_{j \to i}^{(m)}\|_2 + \epsilon. \qquad (19)$$

$$\ell_{ji}^{(m)} = \gamma_m \left[\lambda \frac{|\tilde{s}_{ji}^{(m)}|}{\sqrt{d}} + (1 - \lambda) \operatorname{Re} \left(\frac{\tilde{s}_{ji}^{(m)}}{\tilde{\nu}_{ji}^{(m)}} \right) \right],$$

where $\gamma_m>0$ is a learnable temperature and $\lambda\in[0,1]$ balances magnitude and phase contributions. Because $\widehat{m}_{j\to i}^{(m)}$ is obtained from gauge-equivariant $r_{j\to i}^{(m)}$ via scalar gates, $\widetilde{s}_{ji}^{(m)}$ remains gauge-invariant. The attention weights and aggregated message are

$$\alpha_{ji}^{(m)} = \operatorname{softmax}_{j \in \mathcal{N}(i)} \left(\ell_{ji}^{(m)} \right), \tag{20}$$

$$\widetilde{h}_{i}^{(t+1)} = h_{i}^{(t)} + \sum_{m=1}^{M} \sum_{j \in \mathcal{N}(i)} \alpha_{ji}^{(m)} \widehat{m}_{j \to i}^{(m)}.$$

Readout and Training. We apply node-wise normalization and complex nonlinearity:

$$h_i^{(t+1)} = \text{modReLU}(\text{NodeNorm}(\widetilde{h}_i^{(t+1)})).$$
 (21)

Here, the $NodeNorm(\cdot)$ and $modReLU(\cdot)$ are given by:

$$NodeNorm(h_i) = \frac{h_i - \mu_i}{\varsigma_i + \epsilon},$$
(22)

$$\mathrm{modReLU}(z) = \mathrm{max}(|z|+b,0) \cdot \frac{z}{|z|+\mathbf{1}_{|z|=0}\epsilon},$$

where b is a real-valued learnable bias, $\mu_i = \frac{1}{d} \sum_{k=1}^d h_{ik}$, and $\varsigma_i = \sqrt{\frac{1}{d} \sum_{k=1}^d |h_{ik} - \mu_i|^2}$. For classification, the final complex node representations $h_i^{(L)}$ are mapped to real logits by concatenating their real and imaginary parts, followed by LayerNorm and a linear classifier:

$$z_{i} = \text{vec}\left(\text{Re}(h_{i}^{(L)}), \text{Im}(h_{i}^{(L)})\right) \in \mathbb{R}^{2d},$$

$$\text{logits}_{i} = W_{\text{cls}}\text{Dropout}(\text{LayerNorm}(z_{i})) \in \mathbb{R}^{C}.$$
(23)

We train the model with a cross-entropy loss on labeled nodes V_L :

$$\mathcal{L}_{CE} = -\frac{1}{|\mathcal{V}_L|} \sum_{i \in \mathcal{V}_L} \log p_{\Theta} (y_i \mid \text{logits}_i), \qquad (24)$$

and a Jensen-Shannon consistency term between two stochastic forward passes:

$$\mathcal{L}_{\rm JS} = {\rm JS}\left({\rm softmax}\left({\rm logits}^{(1)}/T\right), \ {\rm softmax}\left({\rm logits}^{(2)}/T\right)\right)$$
(25)

with temperature T > 0. The final training objective is

$$\mathcal{L} = \mathcal{L}_{CE} + \lambda_{IS} \mathcal{L}_{IS}. \tag{26}$$

The overall algorithm, implementation details, and scalability on large graphs are introduced in Appendix A.

5. Theoretical Properties

In this section, we present theoretical justifications for the core design choices introduced in Section 4. Specifically, we show that (i) Self-Interference Cancellation (SIC) attenuates self-parallel components and mitigates low-frequency dominance, (ii) sign-aware gating provides bounded and stable propagation, (iii) complex-valued transport maintains the gauge structure and invariance, and (iv) the resulting GESC layer admits explicit Lipschitz bounds, contributing to robustness against spectral collapse and over-smoothing.

5.1. Why SIC Works: a Linear-Algebraic View

Compared to the prior works (Zhang et al., 2021; He et al., 2022), SIC addresses the accumulation bias, acting as a notch on low-frequency modes in self-aligned directions.

Proposition 5.1 (Effect of SIC on message decomposition). Let $\tilde{h} = \tilde{h}_{\parallel} + \tilde{h}_{\perp}$ with $\tilde{h}_{\parallel} \parallel h_i^{(t)}$ and $\tilde{h}_{\perp} \perp h_i^{(t)}$. Using the Tikhonov-regularized rank-1 operator $\Pi_{\epsilon}(h_i^{(t)})$ in Eq. 11,

$$(I - \eta_{\rm sic} \Pi_{\epsilon}(h_i^{(t)}))\tilde{h} = \left(1 - \eta_{\rm sic} \frac{\|h_i^{(t)}\|_2^2}{\|h_i^{(t)}\|_2^2 + \epsilon}\right) \tilde{h}_{\parallel} + \tilde{h}_{\perp}$$
(27)

Thus, SIC attenuates the self-parallel component while preserving orthogonal ones. Proof is given in Appendix B.1.1.

Lemma 5.2 (Reduction of self-parallel energy). Let $\Pi_{\epsilon}(h_i^{(t)})$ be the Tikhonov-regularized rank-1 projector in Eq. 11, and define the self-parallel energy as below:

$$\mathcal{E}_{\parallel}(x) \coloneqq \left\| \Pi_{\epsilon}(h_i^{(t)}) x \right\|_2^2. \tag{28}$$

For any $\eta_{\rm sic} \in [0,1]$ and any $\tilde{h} \in \mathbb{C}^d$,

$$\mathcal{E}_{\parallel} \left((I - \eta_{\text{sic}} \Pi_{\epsilon}(h_i^{(t)})) \tilde{h} \right) \leq \mathcal{E}_{\parallel}(\tilde{h}) \tag{29}$$

In particular, SIC does not increase the squared magnitude of the component parallel to $h_i^{(t)}$, since $\Pi_{\epsilon}(h_i^{(t)})$ is a positive semidefinite rank-1 projector with operator norm at most 1. This limits the influence of self-reinforcing directions, redistributing attention mass toward more informative neighbors. Proof is given in Appendix B.1.2.

Remark 5.3 (Spectral notch effect). Consider a linearized propagation step with normalized adjacency \tilde{A} and self-loop weight α :

$$h^{(t+1)} \approx \alpha h^{(t)} + \tilde{A}h^{(t)}. \tag{30}$$

Under diffusion-like propagation, the dominant local direction of $h^{(t)}$ tends to align with low-frequency eigenmodes of the graph Laplacian. Applying the self-interference cancellation operator $(I - \eta_{\rm sic}\Pi_\epsilon(h_i^{(t)}))$ before attention attenuates the component of each local message parallel to $h_i^{(t)}$, thereby reducing the energy of these low-frequency modes. Consequently, SIC acts as a node-wise notch filter that suppresses low-frequency dominance and delays spectral collapse as depth increases. A more detailed discussion is provided in Appendix B.1.3.

5.2. Stability from Sign-aware Gating

Sign-aware gating provides an additional mechanism for stabilizing propagation by down-weighting negatively aligned residuals before attention. Below, we prove that the resulting gated messages remain uniformly bounded in norm.

Proposition 5.4 (Per-head boundedness with sign-aware gating). Assume U_{ji} is unitary, $\eta_{\text{sic}} \in [0,1]$, and $\xi_{ji}^{(m)}, g_{ji}^{(m)} \in [0,1]$. Let $\{\alpha_{ji}^{(m)}\}_{j \in \mathcal{N}(i)}$ be the attention weights with $\alpha_{ji}^{(m)} \geq 0$ and $\sum_{j \in \mathcal{N}(i)} \alpha_{ji}^{(m)} = 1$. Then, for any node i and head m.

$$\left\| \sum_{j \in \mathcal{N}(i)} \alpha_{ji}^{(m)} \widehat{m}_{j \to i}^{(m)} \right\|_{2} \le \|W^{(m)}\|_{2} \cdot \max_{j \in \mathcal{N}(i)} \|h_{j}^{(t)}\|_{2}. \tag{31}$$

Proof is given in Appendix B.2.1.

This per-head bound shows that the gated aggregation cannot grow faster than a linear map with operator norm $\|W^{(m)}\|_2$, ensuring stable signal magnitudes even in deep networks. In Theorem 5.8, we combine this with SIC and normalization to obtain an explicit Lipschitz bound.

5.3. Gauge Equivariance and Phase Consistency

A central motivation for introducing complex-valued transport is to ensure the consistency under local rephasing of node embeddings. In standard message passing, scalar aggregation is sensitive to arbitrary sign or phase flips, which can destabilize attention and obscure directional relationships. By contrast, our formulation is gauge-equivariant: local phase transformations affect intermediate representations in a controlled, predictable way, and do not alter the final alignment scores or gating decisions.

Theorem 5.5 (Gauge equivariance). For any choice of nodewise phases $\{\psi_i\}_{i\in\mathcal{V}}$, consider the local U(1) gauge transformation

$$h_i^{(t)} \mapsto h_i^{\prime(t)} = e^{i\psi_i} h_i^{(t)}, \qquad U_{ji} \mapsto U'_{ji} = e^{i(\psi_i - \psi_j)} U_{ji}.$$
(32)

For every head m and edge (j,i), the transported neighbor feature and the SIC residual transform covariantly as

$$\tilde{h}_{j\to i}^{\prime(m)} = e^{i\psi_i} \, \tilde{h}_{j\to i}^{(m)}, \qquad r_{j\to i}^{\prime(m)} = e^{i\psi_i} \, r_{j\to i}^{(m)}.$$
 (33)

Moreover, any scalar alignment score of the form

$$s_{ji}^{(m)}(v) = \left(Q^{(m)}h_i^{(t)}\right)^{\mathrm{H}} v_{j\to i}^{(m)},\tag{34}$$

is gauge-invariant, i.e., $s_{ji}^{\prime(m)}(v')=s_{ji}^{(m)}(v)$ under transformation $v_{j\rightarrow i}^{(m)}\in \big\{\tilde{h}_{j\rightarrow i}^{(m)},\ r_{j\rightarrow i}^{(m)},\ \widehat{m}_{j\rightarrow i}^{(m)}\big\}$. Consequently, the GESC update is gauge-equivariant in the sense that

$$\left\{ h_i^{(t)} \right\}_{i \in \mathcal{V}} \mapsto \left\{ e^{i\psi_i} h_i^{(t)} \right\}_{i \in \mathcal{V}}$$

$$\Longrightarrow \left\{ h_i^{(t+1)} \right\}_{i \in \mathcal{V}} \mapsto \left\{ e^{i\psi_i} h_i^{(t+1)} \right\}_{i \in \mathcal{V}}.$$

$$(35)$$

Proof is given in Appendix B.3.1.

This gauge-equivariance property justifies the use of magnetic transport and complex embeddings: local phase choices at each node do not affect attention scores or gating decisions, ensuring robust and well-defined propagation across arbitrary local phase frames.

5.4. Stability and Non-amplification

We now show that the interference-aware design provides explicit stability guarantees, aligning with the gating and SIC mechanisms described in Section 4.

Proposition 5.6 (Self-component non-amplification). *Consider the linear case (i.e., without nonlinearities or normal-*

ization), with the per-layer update

$$h_i^{(t+1)} = h_i^{(t)} + \sum_{m=1}^{M} \sum_{j \in \mathcal{N}(i)} \alpha_{ji}^{(m)} \, \widehat{m}_{j \to i}^{(m)}, \qquad (36)$$

where $\widehat{m}_{i\to i}^{(m)}$ is defined in Section 4. Then, for any node i,

$$\|\Pi_{\epsilon}(h_{i}^{(t)})h_{i}^{(t+1)}\|_{2} \leq \|\Pi_{\epsilon}(h_{i}^{(t)})h_{i}^{(t)}\|_{2}$$

$$+ \sum_{m=1}^{M} \sum_{j \in \mathcal{N}(i)} \alpha_{ji}^{(m)} \|\Pi_{\epsilon}(h_{i}^{(t)})\tilde{h}_{j \to i}^{(m)}\|_{2}.$$
(37)

In particular, the SIC-processed residuals do not increase the self-parallel component: their contribution in the direction of $h_i^{(t)}$ is always bounded above by that of the ungated transported messages, whose magnitude is controlled by the transported terms. Proof is provided in Appendix B.4.1.

Proposition 5.7 (Stability bound). Let $\alpha_{\max} := \max_{m,i,j} \alpha_{ji}^{(m)}$, $\xi_{\max} := \max_{m,i,j} \xi_{ji}^{(m)}$, and assume the in-degree is bounded by Δ (i.e., $|\mathcal{N}(i)| \leq \Delta \ \forall i$). Then, for each head m and node i,

$$\left\| \sum_{j \in \mathcal{N}(i)} \alpha_{ji}^{(m)} \, \xi_{ji}^{(m)} \left(g_{ji}^{(m)} r_{j \to i}^{(m)} + (1 - g_{ji}^{(m)}) \tilde{h}_{j \to i}^{(m)} \right) \right\|_{2}$$

$$\leq \alpha_{\max} \xi_{\max} \Delta \|W^{(m)}\|_{2} \max_{j \in \mathcal{N}(i)} \|h_{j}^{(t)}\|_{2}.$$
 (38)

This shows that soft gating controls the per-layer amplification factor at the head level, ensuring bounded signal growth. Proof is given in Appendix B.4.2.

Theorem 5.8 (Lipschitz continuity and SIC-aware tightened bound). Assume (i) NodeNorm and modReLU are non-expansive (each is 1-Lipschitz with respect to the ℓ_2 norm), (ii) the magnetic transport U_{ji} is unitary, and (iii) the SIC strength satisfies $0 \le \eta_{\rm sic} \le 1$ so that $\|(I - \eta_{\rm sic}\Pi_{\epsilon}(h_i^{(t)}))\|_2 \le 1$ for all i,t. Let $\alpha_{ji}^{(m)} \le \alpha_{\rm max}$ and suppose the in-degree is bounded by Δ . Then a single GESC layer F is Lipschitz with

$$L_{\text{GESC}} \le 1 + \sum_{m=1}^{M} \alpha_{\text{max}} \Delta \|W^{(m)}\|_{2}.$$
 (39)

Moreover, along the node-wise self-parallel direction span $\{h_i^{(t)}\}$, there exist lower bounds $g_{\min}, \xi_{\min}, \eta_{\min} > 0$ on the applied gates and SIC strength such that

$$L_{\text{GESC}}^{\parallel} \le 1 + \sum_{m=1}^{M} \alpha_{\text{max}} \Delta \left(1 - g_{\text{min}} \xi_{\text{min}} \eta_{\text{min}} \right) \|W^{(m)}\|_{2},$$
(40)

so that the directional Lipschitz factor along self-aligned directions is strictly reduced compared to the case without SIC (i.e., $\eta_{\rm sic}=0$). In particular, SIC does not worsen the worst-case Lipschitz constant and tightens it along self-aligned directions. Further discussion of over-smoothing mitigation and complete proofs is provided in Appendix B.5.

Table 1: (Q1) Node classification accuracy on nine benchmark datasets with **top-3 results**. The comparison includes heterophily-aware models, advanced spectral-filtering methods, and recent state-of-the-art architectures

Dataset	Cora	Citeseer	Pubmed	Actor	Chameleon	Squirrel	Cornell	Texas	Wisconsin
Homophily \mathcal{G}_h (Eq. 1)	0.81	0.74	0.80	0.22	0.23	0.22	0.11	0.06	0.16
GCN (Kipf & Welling, 2017)	$81.4_{\pm 0.71}$	$67.5_{\pm 0.70}$	$79.5_{\pm 0.47}$	$20.3_{\pm 0.46}$	$54.9_{\pm 0.59}$	$31.1_{\pm 0.71}$	$39.9_{\pm 0.79}$	$57.0_{\pm 0.90}$	$49.0_{\pm 0.78}$
GAT (Veličković et al., 2018)	$82.6_{\pm 0.55}$	$68.4_{\pm0.83}$	$79.9_{\pm 0.45}$	$22.8_{\pm0.41}$	$54.4_{\pm0.84}$	$31.0_{\pm 0.93}$	$42.6_{\pm0.80}$	$58.8_{\pm 1.01}$	$50.2_{\pm 0.97}$
H ₂ GCN (Zhu et al., 2020)	$80.3_{\pm 0.52}$	$68.5_{\pm 0.76}$	$78.8_{\pm 0.37}$	$25.9_{\pm 1.07}$	$53.1_{\pm 0.88}$	$31.2_{\pm 0.68}$	$55.0_{\pm 1.15}$	$66.1_{\pm 1.27}$	$62.0_{\pm 1.25}$
SIGN (Frasca et al., 2020)	$82.4_{\pm 0.57}$	$68.6_{\pm 0.70}$	$79.7_{\pm 0.43}$	$22.6_{\pm0.40}$	$54.2_{\pm 0.80}$	$31.2_{\pm 0.94}$	$42.4_{\pm0.85}$	$58.8_{\pm 0.95}$	$50.4_{\pm0.88}$
GCNII (Chen et al., 2020)	$82.2_{\pm 0.64}$	$67.8_{\pm 1.21}$	$79.4_{\pm 0.52}$	$26.2_{\pm 1.22}$	$54.0_{\pm 0.77}$	$30.8_{\pm 0.91}$	$56.0_{\pm 1.27}$	$69.1_{\pm 1.34}$	$63.9_{\pm 1.29}$
MagNet (Zhang et al., 2021)	$83.8_{\pm 0.56}$	$68.9_{\pm 0.67}$	$80.1_{\pm 0.40}$	$26.4_{\pm 0.97}$	$56.9_{\pm 1.34}$	$32.4_{\pm 1.15}$	$55.1_{\pm 1.31}$	$65.3_{\pm 1.46}$	$61.7_{\pm 1.54}$
GPRGNN (Chien et al., 2021)	$82.0_{\pm 0.59}$	$70.1_{\pm 0.91}$	$79.4_{\pm 0.57}$	$25.2_{\pm 0.89}$	$55.8_{\pm0.81}$	$30.6_{\pm 0.63}$	$51.4_{\pm 1.36}$	$60.7_{\pm 1.28}$	$63.1_{\pm 1.21}$
FAGCN (Bo et al., 2021)	$82.8_{\pm 0.66}$	$70.4_{\pm 1.20}$	$79.8_{\pm 0.55}$	$26.8_{\pm 1.24}$	$54.8_{\pm0.81}$	$31.2_{\pm 0.87}$	$56.8_{\pm 1.22}$	69.7 $_{\pm 1.41}$	64.3 $_{\pm 1.25}$
ACM-GCN (Luan et al., 2022)	$82.9_{\pm 0.70}$	$70.7_{\pm 0.81}$	$80.0_{\pm 0.45}$	$25.9_{\pm 1.02}$	$56.6_{\pm 1.40}$	$32.1_{\pm 1.05}$	$55.1_{\pm 1.35}$	$65.9_{\pm 1.52}$	$62.1_{\pm 1.45}$
GloGNN (Li et al., 2022a)	$82.9_{\pm 0.45}$	$70.9_{\pm 0.48}$	80.3 $_{\pm 0.31}$	$27.0_{\pm 0.73}$	$53.9_{\pm 0.70}$	$31.0_{\pm 0.82}$	$48.8_{\pm 1.15}$	$62.5_{\pm 1.21}$	$60.2_{\pm 1.12}$
Auto-HeG (Zheng et al., 2023)	$82.4_{\pm 1.07}$	$70.2_{\pm 1.36}$	$80.1_{\pm 0.27}$	$26.5_{\pm 0.99}$	$54.3_{\pm 1.33}$	$31.7_{\pm 1.11}$	$53.9_{\pm 1.03}$	$67.4_{\pm 1.65}$	$64.0_{\pm 1.49}$
DirGNN (Rossi et al., 2024)	84.6 $_{\pm 0.61}$	71.5 $_{\pm 0.88}$	$80.2_{\pm 0.43}$	$27.5_{\pm 0.95}$	59.8 $_{\pm 1.45}$	$35.2_{\pm 1.13}$	57.9 $_{\pm 1.80}$	$68.8_{\pm 1.57}$	$63.0_{\pm 1.33}$
PCNet (Li et al., 2024)	$83.4_{\pm 0.77}$	$70.8_{\pm 1.15}$	$80.0_{\pm 0.29}$	$26.6_{\pm 0.90}$	$57.6_{\pm 1.65}$	$31.8_{\pm 0.58}$	$54.1_{\pm 1.02}$	$62.5_{\pm 1.16}$	$60.5_{\pm 1.13}$
TFE-GNN (Duan et al., 2024)	84.1 $_{\pm 0.72}$	71.7 $_{\pm 1.14}$	80.3 $_{\pm 0.30}$	$28.1_{\pm 0.81}$	60.2 $_{\pm 1.61}$	$36.0_{\pm 0.59}$	$53.7_{\pm 1.07}$	$63.8_{\pm 1.11}$	$62.5_{\pm 1.19}$
CGNN (Zhuo et al., 2025)	$83.9_{\pm 0.70}$	$70.5_{\pm 1.23}$	$80.1_{\pm 0.51}$	$26.5_{\pm 1.17}$	$59.1_{\pm 0.78}$	$34.4_{\pm 0.97}$	57.4 $_{\pm 1.25}$	70.3 $_{\pm 1.36}$	64.9 $_{\pm 1.22}$
GESC (ours)	84.9 _{±0.54}	72.1 $_{\pm 0.51}$	80.4 _{±0.10}	30.4 _{±0.66}	65.0 $_{\pm 1.29}$	37.9 _{±0.36}	59.4 _{±1.93}	74.5 $_{\pm 1.52}$	66.6 _{±2.14}

6. Experiments

We conduct extensive experiments to evaluate our framework by addressing the following key questions:

- Q1: Accuracy. Does GESC improve node classification performance across both homophilous and heterophilous benchmarks?
- Q2: Ablation Study. How do SIC, sign-aware gating, and gauge-equivariant transport individually contribute to the overall performance?
- Q3: Robustness and Sensitivity. How sensitive is the model to variations in hyperparameters (interference cancellation rate $\eta_{\rm sic}$ and JS divergence $\lambda_{\rm JS}$) in Eq. 11 and 26, and how stable is it under edge perturbations?
- Q4: Over-smoothing. Do the proposed strategies alleviate over-smoothing and maintain stable signal propagation when stacking deeper layers?

The details of Datasets and Baselines are in Appendix C.

6.1. (Q1) Main Results

Table 1 reports the node classification accuracy on nine benchmarks. Classical propagation models such as GCN and GAT maintain competitive accuracy on strongly homophilic graphs (e.g., Cora and Citeseer), yet their effectiveness degrades sharply when edge-label correlation weakens (e.g., Actor or Squirrel). Depth-regularized variants (GCNII and H₂GCN) alleviate over-smoothing but remain prone to overfitting on small-scale WebKB datasets. Methods that incorporate adaptive propagation or global re-weighting consistently outperform vanilla baselines on moderately

heterophilic datasets (Cornell, Texas, Wisconsin), demonstrating the benefit of learned spectral filters and feedback aggregation. However, their advantage diminishes on WebKBs, where long-range spectral components dominate.

Spectral architectures (DirGNN, TFE-GNN, and CGNN) achieve substantial gains in these challenging settings by leveraging edge orientation and spectral calibration to preserve cross-community dependencies. Overall, the proposed GESC exhibits the most balanced and robust performance, ranking first on five benchmarks and within the top three on the remaining four. Its consistent accuracy across both homophilic and heterophilic graphs demonstrates the effectiveness of the proposed self-interference cancellation and sign-aware gating mechanisms, which jointly harmonize local consistency and global structural information while maintaining low variance across random splits.

More experiments on large graphs, link prediction, attention variants, gauge-invariance, SIC projector ablation, and cross-substitution are provided in Appendix D.

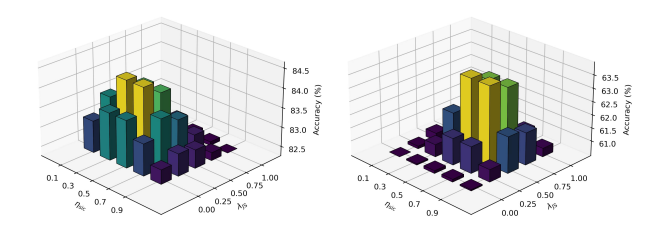
6.2. (Q2) Ablation Study

Table 2 presents the ablation results, where each major component of GESC is removed individually to assess its contribution. Removing the **Self-Interference Cancellation (w/o SIC)** consistently leads to lower accuracy across all benchmarks, verifying that eliminating self-aligned redundant signals before attention effectively mitigates over-smoothing and enhances feature diversity. The **Residual Gating (w/o RG)** mechanism also proves critical, as it adaptively balances constructive and destructive interference. Without RG, accuracy decreases by approximately 1.5-2.0% on average, indicating that the residual gate prevents the amplification of harmful correlations. The absence of **Gauge-Equivariant**

Table 2: (Q2) Ablation study on four benchmark datasets (Accuracy %). Each component is incrementally removed from the full GESC model to analyze its contribution.

Variant	Cora	Citeseer	Chameleon	Texas
w/o SIC	83.5	69.5	62.1	71.2
w/o RG	83.8	70.0	62.6	72.4
w/o GET	83.0	69.2	61.8	70.7
w/o Complex	82.6	68.6	60.9	70.1
Full GESC	84.9	72.1	65.0	74.5

Transport (w/o GET) causes one of the most pronounced performance drops (up to -3.8%), demonstrating that phase-consistent message transport is vital for preserving robustness under sign and orientation perturbations. Finally, replacing complex-valued representations with real-valued ones (w/o Complex) consistently degrades performance, confirming that the coupled magnitude—phase representation provides richer and more expressive relational features than purely real-valued aggregation.



- (a) Cora (homophilic)
- (b) Chameleon (heterophilic)

Figure 3: (Q3) Sensitivity of node classification accuracy to $\eta_{\rm sic}$ (Eq. 11) and $\lambda_{\rm JS}$ (Eq. 26) on the Cora (left) and Chameleon (right) datasets. The z-axis is normalized relative to the minimum accuracy for each graph

6.3. (Q3) Robustness and Sensitivity

To assess the robustness of GESC, we analyze its sensitivity to two key hyperparameters: the information coupling coefficient $\eta_{\rm sic}$ and the joint-smoothing regularizer $\lambda_{\rm JS}$. Figure 3 illustrates the node classification accuracy landscape over $(\eta_{\rm sic}, \lambda_{\rm JS})$ for the Cora and Chameleon datasets. The response surfaces exhibit smooth, convex-like patterns centered around the optimal region, indicating stable convergence behavior under small perturbations of either hyperparameter. Even when $\eta_{\rm sic}$ or $\lambda_{\rm JS}$ deviates from their optimal values, the performance drop remains moderate (within 1-2%), demonstrating that the model maintains high accuracy without precise tuning. This stability stems from the complementary effects of self-interference cancellation and residual gating, which jointly regulate the balance between local smoothing and global consistency. Overall,

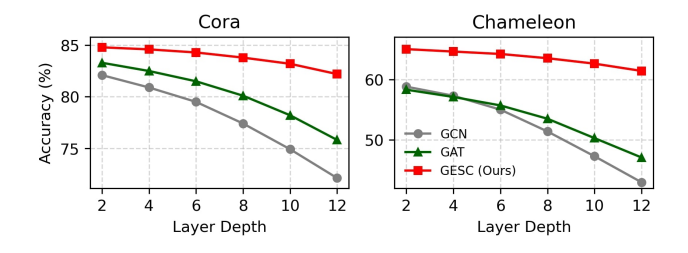


Figure 4: (Q4) Node classification accuracy versus network depth on the Cora (left) and Chameleon (right) datasets using GCN, GAT, and the proposed GESC

these results confirm that GESC achieves robust generalization across diverse graph structures with minimal sensitivity to hyperparameter selection.

6.4. (Q4) Over-smoothing

To evaluate the effect of network depth, we analyze whether GESC mitigates the over-smoothing problem common in deep message-passing networks. As the number of layers increases, standard GCN and GAT models exhibit a sharp decline in accuracy due to feature homogenization across nodes, leading to indistinguishable embeddings. Figure 4 shows node classification accuracy on Cora and Chameleon when stacking up to 12 layers. In both datasets, GCN and GAT suffer progressive degradation with depth, confirming the accumulation of over-smoothed signals. In contrast, GESC maintains consistently higher accuracy, indicating that self-interference cancellation and residual gating effectively stabilize propagation and preserve discriminative information in deep architectures. This depth robustness arises from the interplay between local refinement and global consistency enforced by gauge-equivariant transport, preventing representation collapse as the network grows deeper.

7. Conclusion

We presented GESC, a gauge-equivariant graph neural network that replaces additive message passing with a principled wave-interference mechanism. The self-interference cancellation suppresses redundant self-reinforcement, while sign-aware gating balances constructive and destructive interference through alignment. Theoretically, GESC guarantees gauge and permutation equivariance, mitigates oversmoothing, and maintains Lipschitz stability via spectral orthogonalization. Empirically, it achieves consistent improvements across both homophilous and heterophilous benchmarks, demonstrating robust and interpretable propagation dynamics. Beyond these results, GESC provides a geometric foundation for interference-aware graph learning, paving the way toward deeper, physically grounded models that unify topology, symmetry, and signal propagation.

Impact Statement

This paper aims to advance the field of graph representation learning by introducing a principled framework for interference-aware and gauge-equivariant message passing. Potential benefits include more reliable node-level inference and better modeling of directional or oscillatory interactions. GESC targets semi-supervised node classification under homophily/heterophily and is not a drop-in solution for safety-critical or privacy-sensitive tasks without additional safeguards. We do not foresee any specific negative societal consequences directly resulting from this work.

References

- Abu-El-Haija, S., Perozzi, B., Kapoor, A., Alipourfard, N., Lerman, K., Harutyunyan, H., Ver Steeg, G., and Galstyan, A. Mixhop: Higher-order graph convolutional architectures via sparsified neighborhood mixing. In *In*ternational Conference on Machine Learning (ICML), 2019.
- Alon, U. and Yahav, E. On the bottleneck of graph neural networks and its practical implications. In *International Conference on Learning Representations*, 2021.
- Black, M., Wan, Z., Nayyeri, A., and Wang, Y. Understanding oversquashing in gnns through the lens of effective resistance. In *International Conference on Machine Learning*, pp. 2528–2547. PMLR, 2023.
- Bo, D., Wang, X., and Shi, C. Beyond low-frequency information in graph convolutional networks. In *AAAI*, 2021.
- Brandstetter, J., Welling, M., and Weiler, M. Geometric and physical quantities improve e(3) equivariant message passing. In *International Conference on Learning Representations (ICLR)*, 2022.
- Bronstein, M. M., Bruna, J., Cohen, T. S., and Veličković, P. Geometric deep learning: Grids, groups, graphs, geodesics, and gauges. *arXiv preprint arXiv:2104.13478*, 2021.
- Chen, M., Wei, Z., Huang, Z., Ding, B., and Li, Y. Simple and deep graph convolutional networks. In *International conference on machine learning*, pp. 1725–1735. PMLR, 2020.
- Chien, E., Pan, C.-K., Peng, W.-C., and Milenkovic, O. Adaptive universal generalized pagerank graph neural network. In *ICLR*, 2021.
- Choi, Y., Ko, T., Choi, J., and Kim, C.-K. Beyond binary: Improving signed message passing in graph neural networks for multi-class graphs. *IEEE Transactions on Pattern Analysis and Machine Intelligence*, 2025a.

- Choi, Y., Ko, T., Choi, J., and Kim, C.-K. Selective blocking for message-passing neural networks on heterophilic graphs. In *The 41st Conference on Uncertainty in Artificial Intelligence*, 2025b.
- Cohen, T. S. and Welling, M. Group equivariant convolutional networks. In *International Conference on Machine Learning (ICML)*, 2016.
- Cohen, T. S., Geiger, M., Köhler, J., and Welling, M. Gauge equivariant convolutional networks and the icosahedral cnn. In *ICML*, 2019.
- de Haan, P., Cohen, T. S., and Welling, M. Gauge equivariant mesh cnns: Anisotropic convolutions on geometric graphs. In *International Conference on Learning Representations (ICLR)*, 2021.
- Defferrard, M., Bresson, X., and Vandergheynst, P. Convolutional neural networks on graphs with fast localized spectral filtering. In *NeurIPS*, 2016.
- Derr, T., Ma, Y., and Tang, J. Signed graph convolutional networks. In *IEEE International Conference on Data Mining (ICDM)*, 2018.
- Du, L., Shi, X., Fu, Q., Ma, X., Liu, H., Han, S., and Zhang, D. Gbk-gnn: Gated bi-kernel graph neural networks for modeling both homophily and heterophily. In *Proceedings of the ACM web conference* 2022, pp. 1550–1558, 2022.
- Duan, R., Guang, M., Wang, J., Yan, C., Qi, H., Su, W., Tian, C., and Yang, H. Unifying homophily and heterophily for spectral graph neural networks via triple filter ensembles. Advances in Neural Information Processing Systems, 37: 93540–93567, 2024.
- Frasca, F., Rossi, E., Eynard, D., Chamberlain, B., Bronstein, M., and Monti, F. Sign: Scalable inception graph neural networks. *arXiv preprint arXiv:2004.11198*, 2020.
- Gasteiger, J., Weißenberger, S., and Günnemann, S. Diffusion improves graph learning. In *Advances in Neural Information Processing Systems (NeurIPS)*, 2019.
- Gilmer, J., Schoenholz, S. S., Riley, P. F., Vinyals, O., and Dahl, G. E. Neural message passing for quantum chemistry. In *ICML*, 2017.
- He, M., Wei, Z., Huang, Z., and Xu, H. Bernnet: Learning arbitrary graph spectral filters via bernstein approximation. In *Advances in Neural Information Processing Systems (NeurIPS)*, 2021.
- He, Y., Perlmutter, M., Reinert, G., and Cucuringu, M. Msgnn: A spectral graph neural network based on a novel magnetic signed laplacian. In *Proceedings of the First*

- Learning on Graphs Conference (PMLR 198), pp. 40:1–40:39, 2022.
- Huang, J., Shen, J., Hou, R., Liu, S., and Ma, X. Signed graph attention networks. In *ICLR*, 2019.
- Jin, W. et al. Universal spectral graph neural networks. In NeurIPS, 2021.
- Kipf, T. N. and Welling, M. Variational graph auto-encoders. *arXiv preprint arXiv:1611.07308*, 2016.
- Kipf, T. N. and Welling, M. Semi-supervised classification with graph convolutional networks. *ICLR*, 2017.
- Klicpera, J., Bojchevski, A., and Günnemann, S. Predict then propagate: Graph neural networks meet personalized pagerank. In *International Conference on Learning Representations (ICLR)*, 2019.
- Ko, T., Choi, Y., and Kim, C.-K. A spectral graph convolution for signed directed graphs via magnetic laplacian. *Neural Networks*, 164:562–574, 2023.
- Levie, R., Monti, F., Bresson, X., and Bronstein, M. M. Cayleynets: Graph convolutional neural networks with complex rational spectral filters. In *International Confer*ence on Learning Representations, 2018.
- Li, B., Pan, E., and Kang, Z. Pc-conv: Unifying homophily and heterophily with two-fold filtering. In *Proceedings of the AAAI conference on artificial intelligence*, volume 38, pp. 13437–13445, 2024.
- Li, Q., Han, Z., and Wu, X.-M. Deeper insights into graph convolutional networks for semi-supervised learning. In *AAAI*, 2018.
- Li, X., Zhu, R., Cheng, Y., Shan, C., Luo, S., Li, D., and Qian, W. Finding global homophily in graph neural networks when meeting heterophily. In *International conference on machine learning*, pp. 13242–13256. PMLR, 2022a.
- Li, X. et al. Learning signed graphs with attention. In *WWW*, 2022b.
- Lim, D., Hohne, F., Li, X., Huang, S. L., Gupta, V., Bhalerao, O., and Lim, S.-N. Large scale learning on non-homophilous graphs: New benchmarks and strong simple methods. In *Advances in Neural Information Pro*cessing Systems (NeurIPS), 2021.
- Lim, D., Robinson, J., Zhao, L., Smidt, T., Sra, S., Maron, H., and Jegelka, S. Sign and basis invariant networks for spectral graph representation learning. arXiv preprint arXiv:2202.13013, 2022.

- Luan, S., Hua, C., Lu, Q., Zhu, J., Zhao, M., Zhang, S., Chang, X.-W., and Precup, D. Revisiting heterophily for graph neural networks. *Advances in neural information* processing systems, 35:1362–1375, 2022.
- Luo, D., Yuan, S., Stokes, J., and Clark, B. K. Gauge equivariant neural networks for 2+ 1d u (1) gauge theory simulations in hamiltonian formulation. *arXiv* preprint *arXiv*:2211.03198, 2022.
- Ma, X., Liu, Y., Zhang, C., and Li, P. Simplifying and empowering transformers for large-scale graph learning. In *Advances in Neural Information Processing Systems* (NeurIPS), 2021.
- Marques, A. G., Segarra, S., and Mateos, G. Signal processing on directed graphs: The role of edge directionality when processing and learning from network data. *IEEE Signal Processing Magazine*, 37(6):99–116, 2020.
- Oono, K. and Suzuki, T. Graph neural networks exponentially lose expressive power for node classification. In *ICLR*, 2019.
- Pei, H., Wei, B., Chang, K. C.-C., Lei, Y., and Yang, B. Geom-gcn: Geometric graph convolutional networks. In *International Conference on Learning Representations* (*ICLR*), 2020.
- Rampášek, L., Galkin, M., Lange, H., Jain, S., Chen, G. W., and Beaini, D. Recipe for a general, powerful, scalable graph transformer. In *International Conference on Learn*ing Representations, 2022.
- Rong, Y., Huang, W., Xu, T., and Huang, J. Dropedge: Towards deep graph convolutional networks on node classification. *arXiv* preprint arXiv:1907.10903, 2019.
- Rossi, E., Charpentier, B., Di Giovanni, F., Frasca, F., Günnemann, S., and Bronstein, M. M. Edge directionality improves learning on heterophilic graphs. In *Learning on graphs conference*, pp. 25–1. PMLR, 2024.
- Rozemberczki, B., Davies, R., Sarkar, R., and Sutton, C. Gemsec: Graph embedding with self clustering. In *Proceedings of the 2019 IEEE/ACM international conference on advances in social networks analysis and mining*, pp. 65–72, 2019.
- Rusch, T. K. and Mishra, S. Coupled oscillatory recurrent neural network (cornn): An accurate and (gradient) stable architecture for learning long time dependencies. *arXiv* preprint arXiv:2010.00951, 2020.
- Sun, Z., Deng, Z.-H., Nie, J.-Y., and Tang, J. Rotate: Knowledge graph embedding by relational rotation in complex space. In *ICLR*, 2019.

- Trouillon, T., Welbl, J., Riedel, S., Gaussier, E., and Bouchard, G. Complex embeddings for simple link prediction. In *ICML*, 2016.
- Veličković, P., Cucurull, G., Casanova, A., Romero, A., Liò, P., and Bengio, Y. Graph attention networks. In *ICLR*, 2018.
- Wang, Y. and Derr, T. Tree decomposed graph neural network. In *Proceedings of the 30th ACM international conference on information & knowledge management*, pp. 2040–2049, 2021.
- Wang, Y., Wang, Y., Yang, J., and Lin, Z. Dissecting the diffusion process in linear graph convolutional networks. Advances in Neural Information Processing Systems, 34: 5758–5769, 2021.
- Wu, Z., Pan, S., Chen, F., Long, G., Zhang, C., and Yu, P. S. A comprehensive survey on graph neural networks. *IEEE Transactions on Neural Networks and Learning Systems*, 2019.
- Xu, K., Hu, W., Leskovec, J., and Jegelka, S. How powerful are graph neural networks? In *International Conference on Learning Representations*, 2019.
- Yan, J., Wang, Y., Wang, Q., He, W., and Pan, S. Two sides of the same coin: Heterophily and oversmoothing in graph convolutional neural networks. In *Proceedings of the AAAI Conference on Artificial Intelligence*, 2022.
- Zhang, S., Tong, H., Xu, J., and Maciejewski, R. Graph convolutional networks: a comprehensive review. *Computational Social Networks*, 6(1):1–23, 2019.
- Zhang, X., Bu, J., Zhu, Z., Xuan, Q., and Yu, Z. Magnet: A neural network for directed graphs. In *NeurIPS*, 2021.
- Zhang, Y., Yuan, H., Li, H., Wei, C., and Yao, C. Complex-valued graph neural network on space target classification for defocused isar images. *IEEE Geoscience and Remote Sensing Letters*, 19:1–5, 2022.
- Zheng, X., Ma, T., Guo, H., and Wang, R. Graph neural networks for graphs with heterophily: A survey. *arXiv* preprint arXiv:2202.07082, 2022.
- Zheng, X., Zhang, M., Chen, C., Zhang, Q., Zhou, C., and Pan, S. Auto-heg: Automated graph neural network on heterophilic graphs. In *Proceedings of the ACM Web Conference 2023*, pp. 611–620, 2023.
- Zhu, J., Yan, Y., Zhao, L., Heimann, M., Akoglu, L., and Koutra, D. Beyond homophily in graph neural networks: Current limitations and effective designs. *Advances in neural information processing systems*, 33:7793–7804, 2020.

Zhuo, W., Yu, H., Tan, G., and Li, X. Commute graph neural networks. In Singh, A., Fazel, M., Hsu, D., Lacoste-Julien, S., Berkenkamp, F., Maharaj, T., Wagstaff, K., and Zhu, J. (eds.), *Proceedings of the 42nd International Conference on Machine Learning*, volume 267 of *Proceedings of Machine Learning Research*, pp. 80612–80628. PMLR, 13–19 Jul 2025. URL https://proceedings.mlr.press/v267/zhuo25a.html.

A. Algorithmic and Implementation Details

A.1. Overall Algorithm

```
Algorithm 1 GESC: Gauge-Equivariant Self-Interference Cancellation (one training epoch)
```

```
Require: Graph \mathcal{G} = (\mathcal{V}, \mathcal{E}), real features H_{\text{real}}^{(0)}, labels Y; hyperparameters \{L, M, \{\gamma_m\}_{m=1}^M, \lambda, \eta_{\text{sic}}, \epsilon, p_{\text{edge-drop}}, T, \lambda_{\text{JS}}\}
 Ensure: Updated parameters \Theta
   1: Complex lift: H^{(0)} \leftarrow H^{(0)}_{\rm real} W^{(0)}_{\rm re} + i H^{(0)}_{\rm real} W^{(0)}_{\rm im}
2: Magnetic transports: For (j \rightarrow i) \in \mathcal{E}, set U_{ji} = e^{i\theta_{ji}} (unit-modulus)
                  H^{(\ell)} \leftarrow 0 {accumulator (same shape as H^{(\ell-1)})}
                  for m=1 to M do
   5:
                         for all (j \to i) \in \mathcal{E} do
   6:
                               Source transport and SIC projector: \tilde{h}_{j \to i}^{(m)} \leftarrow U_{ji} W^{(m)} h_j^{(\ell-1)}, \Pi_{\epsilon}(h_i^{(\ell-1)}) \leftarrow \frac{h_i^{(\ell-1)} (h_i^{(\ell-1)})^H}{\|h_i^{(\ell-1)}\|_2^2 + \epsilon}
   7:
                              \begin{aligned} & \textbf{Self-interference cancellation:} \ r_{j \to i}^{(m)} \leftarrow \tilde{h}_{j \to i}^{(m)} - \eta_{\mathrm{sic}} \cdot \Pi_{\epsilon}(h_i^{(\ell-1)}) \tilde{h}_{j \to i}^{(m)} \\ & \textbf{Pre-gate complex score:} \ s_{ji}^{(m)} \leftarrow (Q^{(m)} h_i^{(\ell-1)})^H \, r_{j \to i}^{(m)} \\ & \textbf{Gate normalizer:} \ \nu_{ji,\mathrm{gate}}^{(m)} \leftarrow \|Q^{(m)} h_i^{(\ell-1)}\|_2 \cdot \|r_{j \to i}^{(m)}\|_2 + \epsilon \\ & \textbf{Phase-consistent alignment:} \ \rho_{ji}^{(m)} \leftarrow \mathrm{Re} \left(\frac{s_{ji}^{(m)}}{\nu_{ji,\mathrm{gate}}^{(m)}}\right) \end{aligned}
   8:
   9:
 10:
11:
                              Sign-aware gate and residual: \xi_{ji}^{(m)} \leftarrow \sigma(c_m \, \rho_{ji}^{(m)} + d_m) \,, \quad \bar{r}_{j \to i}^{(m)} \leftarrow \xi_{ji}^{(m)} \, r_{j \to i}^{(m)} Residual gate: x_{ji}^{(m)} \leftarrow \left[\log(1 + \|\bar{r}_{j \to i}^{(m)}\|_2), \, \log(1 + \|\tilde{h}_{j \to i}^{(m)}\|_2), \, \log(1 + |s_{ji}^{(m)}|)\right], \quad g_{ji}^{(m)} \leftarrow \sigma(a_m^\top x_{ji}^{(m)} + b_m) Post-gate message and score: \widehat{m}_{j \to i}^{(m)} \leftarrow g_{ji}^{(m)} \, \bar{r}_{j \to i}^{(m)} + \left(1 - g_{ji}^{(m)}\right) \, \tilde{h}_{j \to i}^{(m)}, \quad \widetilde{s}_{ji}^{(m)} \leftarrow (Q^{(m)} h_i^{(\ell-1)})^H \, \widehat{m}_{j \to i}^{(m)} Attention normalizer: \nu_{ji, \text{attn}}^{(m)} \leftarrow \|Q^{(m)} h_i^{(\ell-1)}\|_2 \cdot \|\widehat{m}_{j \to i}^{(m)}\|_2 + \epsilon
 12:
13:
 14:
 15:
                               Hybrid attention logit: \ell_{ji}^{(m)} \leftarrow \gamma_m \left[ \lambda \frac{|\tilde{s}_{ji}^{(m)}|}{\sqrt{d}} + (1 - \lambda) \operatorname{Re} \left( \frac{\tilde{s}_{ji}^{(m)}}{\nu_{ii \text{ attn}}^{(m)}} \right) \right]
 16:
17:
                         end for
                         for all i \in \mathcal{V} do
 18:
                               Attention: \alpha_{ji}^{(m)} \leftarrow \operatorname{softmax}_{j \in \mathcal{N}(i)} \left( \ell_{ji}^{(m)} \right)
 19:
20:
                         for all (j \to i) \in \mathcal{E} do
21:
                               Aggregate (head-m): H_i^{(\ell)} += \alpha_{ii}^{(m)} \widehat{m}_{i\rightarrow j}^{(m)}
22:
                         end for
23:
                  end for
24:
                  Residual update: \widetilde{h}_i^{(\ell)} \leftarrow h_i^{(\ell-1)} + H_i^{(\ell)} \quad \forall i
25:
                  Node-wise stats (on \widetilde{h}_i^{(\ell)}): \mu_i \leftarrow \frac{1}{d} \sum_k \widetilde{h}_{ik}^{(\ell)}, \ \ \sigma_i \leftarrow \sqrt{\frac{1}{d} \sum_k |\widetilde{h}_{ik}^{(\ell)} - \mu_i|^2}
26:
                  NodeNorm and Complex activation: NN(i) \leftarrow (\widetilde{h}_i^{(\ell)} - \mu_i)/(\sigma_i + \epsilon), h_i^{(\ell)} \leftarrow \text{modReLU(NN}(i)) \quad \forall i
27:
28: end for
           Readout (real classifier):
30: z_i \leftarrow \text{vec}(\text{Re}(h_i^{(L)}), \text{Im}(h_i^{(L)})); \quad \text{logits}_i \leftarrow W_{\text{cls}} \text{ LayerNorm}(\text{Dropout}(z_i))
31: Cross-entropy: \mathcal{L}_{\text{CE}} \leftarrow -\frac{1}{|\mathcal{V}_L|} \sum_{i \in \mathcal{V}_L} \log p_{\Theta}(y_i \mid \text{logits}_i)
32: JS consistency with edge dropout:
                  Sample two independent edge-drop masks with prob p_{\text{edge-drop}} and re-run forward to get logits^{(1)}, logits^{(2)}
33:
                  \mathcal{L}_{JS} \leftarrow JS\left(\text{softmax}\left(\text{logits}^{(1)}/T\right), \text{ softmax}\left(\text{logits}^{(2)}/T\right)\right)
35: Total loss: \mathcal{L} \leftarrow \mathcal{L}_{CE} + \lambda_{JS} \mathcal{L}_{JS}
 36: Update: \Theta \leftarrow \text{OPTIMIZERSTEP}(\Theta, \nabla_{\Theta} \mathcal{L})
```

A.2. Implementation Details

All experiments are implemented in PyTorch Geometric with complex-valued extensions for message passing. We train all models using the Adam optimizer with a learning rate of 1×10^{-3} and weight decay 5×10^{-4} . A single NVIDIA Titan Xp GPU is used for all experiments. Following Kipf & Welling (2017), we use 20 labeled nodes per class for training and randomly split the remaining nodes into validation and test sets (50%/50%). Early stopping is applied with patience 100 based on validation accuracy. All experiments are repeated over 10 random seeds to report the mean and standard deviation.

Model structure and propagation. Each GESC layer consists of (i) complex linear projection, (ii) gauge-equivariant transport, (iii) self-interference cancellation (SIC), and (iv) sign-aware gating with magnitude-phase attention. The transport U_{ji} is represented as a phase vector and applied through elementwise complex multiplication during edge aggregation. The SIC projection is implemented as a Tikhonov-regularized rank-1 projection

$$P_i^{\perp} = I - \eta_{\rm sic} \Pi_{\epsilon}(h_i), \tag{41}$$

computed via a single complex inner product and outer product per edge. This operation is fused with message construction to avoid redundant memory access. Gating and attention weights are computed in parallel from real-valued scalar magnitudes and normalized with degree-wise softmax.

Sparse and parallel computation. All message passing operations are performed with sparse gather/scatter primitives. Phase transport and SIC are vectorized over edges to minimize per-edge kernel launches, and multi-head attention is parallelized across heads using fused CUDA kernels. The resulting computational complexity scales linearly with the number of edges E up to the d^2 term from complex projections, as analyzed in Section A.3.

A.3. Scalability on Large Graphs

For each head m, one GESC layer involves several computational steps. First, applying the complex linear transform $W^{(m)} \in \mathbb{C}^{d \times d}$ to all source embeddings costs $O(Ed^2)$ when performed directly on edge-stacked features, or alternatively $O(Nd^2)$ if $HW^{(m)}$ is precomputed once plus O(Ed) for subsequent gather operations. Next, the SIC projection requires, for each edge (j,i), computing the scalar $(h_i^*\tilde{h}_{j \to i})$ and removing its parallel component, which involves one complex inner product and one scalar-vector multiply, resulting in O(d) per edge and a total of O(Ed). Attention computation, including magnitude calculation and degree-wise softmax normalization, adds O(E), while message formation and aggregation contribute another O(Ed). Summing these components and multiplying by M attention heads, the overall forward complexity is $O(MEd^2)$, where the d^2 term arises from the complex linear transformations. Since E typically scales much larger than N in real-world sparse graphs and the hidden dimension d remains moderate, this term dominates the runtime.

B. Theoretical Proof

B.1. Why SIC Works: a Linear-Algebraic View

B.1.1. Proof of Proposition 5.1

Let us define $\tilde{h}=\tilde{h}_{\parallel}+\tilde{h}_{\perp}$ with $\tilde{h}_{\parallel}\in\mathrm{span}\{h_{i}^{(t)}\}$ and $\langle h_{i}^{(t)},\tilde{h}_{\perp}\rangle_{\mathbb{C}}=0$. By definition, we can easily infer that

$$\Pi_{\epsilon}(h_i^{(t)}) = \frac{h_i^{(t)} h_i^{(t)H}}{\|h_i^{(t)}\|_2^2 + \epsilon} \tag{42}$$

is a rank-1 linear map. Since $\tilde{h}_{\parallel}=rac{h_i^{(t)}h_i^{(t)H}}{\|h_i^{(t)}\|_2^2}\tilde{h}_{\parallel}$, we have

$$\Pi_{\epsilon}(h_i^{(t)})\tilde{h}_{\parallel} = \frac{\|h_i^{(t)}\|_2^2}{\|h_i^{(t)}\|_2^2 + \epsilon}\tilde{h}_{\parallel}.$$
(43)

The orthogonality gives $h_i^{(t)H} \tilde{h}_\perp = 0$, and thus, $\Pi_\epsilon(h_i^{(t)}) \tilde{h}_\perp = 0$. By linearity,

$$(I - \eta_{\rm sic} \Pi_{\epsilon}(h_i^{(t)}))\tilde{h} = \left(1 - \eta_{\rm sic} \frac{\|h_i^{(t)}\|_2^2}{\|h_i^{(t)}\|_2^2 + \epsilon}\right) \tilde{h}_{\parallel} + \tilde{h}_{\perp},\tag{44}$$

which shows that only the self-parallel component is attenuated while the orthogonal component is preserved. \Box

B.1.2. PROOF OF LEMMA 5.2

Let $\lambda \coloneqq \frac{\|h_i^{(t)}\|_2^2}{\|h_i^{(t)}\|_2^2 + \epsilon} \in (0,1)$ be the nonzero eigenvalue of $\Pi_{\epsilon}(h_i^{(t)})$. Since $\Pi_{\epsilon}(h_i^{(t)})$ is a positive semidefinite rank-1 projector, the following equality holds:

$$\Pi_{\epsilon}(h_i^{(t)})^2 = \lambda \,\Pi_{\epsilon}(h_i^{(t)}). \tag{45}$$

Writing $\tilde{h}_{\parallel} = \Pi_{\epsilon}(h_i^{(t)})\tilde{h}$, SIC gives

$$\Pi_{\epsilon}(h_i^{(t)})(I - \eta_{\rm sic}\Pi_{\epsilon}(h_i^{(t)}))\tilde{h} = (1 - \eta_{\rm sic}\lambda)\,\tilde{h}_{\parallel}.\tag{46}$$

Therefore.

$$\|\Pi_{\epsilon}(h_i^{(t)})(I - \eta_{\rm sic}\Pi_{\epsilon}(h_i^{(t)}))\tilde{h}\|_2^2 = (1 - \eta_{\rm sic}\lambda)^2 \|\tilde{h}_{\parallel}\|_2^2.$$
(47)

Since $0 \le \eta_{\rm sic} \le 1$ and $0 < \lambda < 1$, we have $(1 - \eta_{\rm sic}\lambda)^2 \le 1$. Injecting this inequality into the above equation leads to the following condition:

$$\mathcal{E}_{\parallel}((I - \eta_{\rm sic}\Pi_{\epsilon}(h_i^{(t)}))\tilde{h}) \le \mathcal{E}_{\parallel}(\tilde{h}). \tag{48}$$

Thus, SIC does not increase the squared magnitude of the self-parallel component. \Box

B.1.3. DISCUSSION FOR REMARK 5.3

Let $h^{(t)} = \sum_k c_k^{(t)} u_k$ be the expansion of node features in the Laplacian eigenbasis $\{u_k\}$. For normalized adjacency \tilde{A} , we have

$$\tilde{A}u_k = \mu_k u_k,\tag{49}$$

with eigenvalues $\mu_k \in [-1,1]$, where low-frequency modes correspond to larger μ_k . Then, a diffusion-like propagation $h^{(t+1)} \approx \alpha h^{(t)} + \tilde{A}h^{(t)}$ yields

$$c_k^{(t+1)} \approx (\alpha + \mu_k) c_k^{(t)},\tag{50}$$

implying that low-frequency coefficients are preferentially amplified. Lastly, applying SIC introduces a local filtering term

$$(I - \eta_{\rm sic} \Pi_{\epsilon}(h_i^{(t)})), \tag{51}$$

which, by Proposition 5.1, suppresses components parallel to $h_i^{(t)}$. When $h^{(t)}$ has aligned with low-frequency modes, SIC locally attenuates these directions, acting as a node-wise notch filter and delaying spectral collapse. This reasoning is heuristic and reflects the frequency-selective interpretation of SIC rather than a strict global spectral theorem. \Box

B.2. Stability from Sign-aware Gating

B.2.1. Proof of Proposition 5.4

Fix a head m and a target node i. Recall that

$$\tilde{h}_{j\to i}^{(m)} = U_{ji} W^{(m)} h_j^{(t)}, \tag{52}$$

with U_{ii} unitary,

$$r_{j\to i}^{(m)} = (I - \eta_{\rm sic} \Pi_{\epsilon}(h_i^{(t)})) \tilde{h}_{j\to i}^{(m)}, \quad \bar{r}_{j\to i}^{(m)} = \xi_{ji}^{(m)} r_{j\to i}^{(m)}, \tag{53}$$

and

$$\widehat{m}_{j \to i}^{(m)} = g_{ji}^{(m)} \bar{r}_{j \to i}^{(m)} + (1 - g_{ji}^{(m)}) \tilde{h}_{j \to i}^{(m)}, \tag{54}$$

where $\xi_{ji}^{(m)}, g_{ji}^{(m)} \in [0,1]$. Given that U_{ji} is unitary, the transport bound is defined as

$$\|\tilde{h}_{i\to i}^{(m)}\|_2 = \|U_{ii}W^{(m)}h_i^{(t)}\|_2 = \|W^{(m)}h_i^{(t)}\|_2 \le \|W^{(m)}\|_2\|h_i^{(t)}\|_2.$$
(55)

Through this, we can show the non-expansiveness property of SIC using the Tikhonov-regularized rank-1 operator:

$$\Pi_{\epsilon}(h_i^{(t)}) = \frac{h_i^{(t)}(h_i^{(t)})^{\mathcal{H}}}{\|h_i^{(t)}\|_2^2 + \epsilon},\tag{56}$$

which is Hermitian and PSD with eigenvalues $\left\{\frac{\|h_i^{(t)}\|_2^2}{\|h_i^{(t)}\|_2^2+\epsilon}, 0, \dots, 0\right\}$. This property shows that $\|\Pi_{\epsilon}(h_i^{(t)})\|_2 \le 1$. Since the following inequality holds

$$||I - \eta_{\text{sic}}\Pi_{\epsilon}(h_i^{(t)})||_2 < 1,$$
 (57)

for $0 \le \eta_{\rm sic} \le 1$, and thus,

$$||r_{j\to i}^{(m)}||_2 = ||(I - \eta_{\rm sic}\Pi_{\epsilon}(h_i^{(t)}))\tilde{h}_{j\to i}^{(m)}||_2 \le ||\tilde{h}_{j\to i}^{(m)}||_2.$$
(58)

Now, we delve into the sign-aware scaling and residual mixing. Since $0 \le \xi_{ii}^{(m)} \le 1$,

$$\|\bar{r}_{j\to i}^{(m)}\|_2 = \|\xi_{ji}^{(m)}r_{j\to i}^{(m)}\|_2 \le \|r_{j\to i}^{(m)}\|_2 \le \|\tilde{h}_{j\to i}^{(m)}\|_2.$$

$$(59)$$

Moreover, $0 \le g_{ji}^{(m)} \le 1$ implies that $\widehat{m}_{j \to i}^{(m)}$ is a convex combination of $\bar{r}_{j \to i}^{(m)}$ and $\tilde{h}_{j \to i}^{(m)}$. Consequently,

$$\|\widehat{m}_{j\to i}^{(m)}\|_{2} \le g_{ji}^{(m)} \|\bar{r}_{j\to i}^{(m)}\|_{2} + (1 - g_{ji}^{(m)}) \|\widetilde{h}_{j\to i}^{(m)}\|_{2} \le \|\widetilde{h}_{j\to i}^{(m)}\|_{2}. \tag{60}$$

The last term is about attention aggregation. Let $\{\alpha_{ji}^{(m)}\}_{j\in\mathcal{N}(i)}$ be the attention weights with $\alpha_{ji}^{(m)}\geq 0$ and $\sum_{j\in\mathcal{N}(i)}\alpha_{ji}^{(m)}=1$. By the triangle inequality and convexity (a weighted average is bounded by the maximum term), one can introduce:

$$\left\| \sum_{j \in \mathcal{N}(i)} \alpha_{ji}^{(m)} \widehat{m}_{j \to i}^{(m)} \right\|_{2} \le \sum_{j \in \mathcal{N}(i)} \alpha_{ji}^{(m)} \|\widehat{m}_{j \to i}^{(m)}\|_{2} \le \max_{j \in \mathcal{N}(i)} \|\widehat{m}_{j \to i}^{(m)}\|_{2} \le \max_{j \in \mathcal{N}(i)} \|\widetilde{h}_{j \to i}^{(m)}\|_{2}.$$
(61)

Combining with Eq. 52 yields

$$\left\| \sum_{j \in \mathcal{N}(i)} \alpha_{ji}^{(m)} \widehat{m}_{j \to i}^{(m)} \right\|_{2} \le \|W^{(m)}\|_{2} \cdot \max_{j \in \mathcal{N}(i)} \|h_{j}^{(t)}\|_{2}, \tag{62}$$

which proves the claim. \square

B.3. Gauge Equivariance and Phase Consistency

B.3.1. Proof of Theorem 5.5

Let local U(1) gauge transformations act as

$$h_i^{(t)} \mapsto h_i^{\prime(t)} = e^{i\psi_i} h_i^{(t)}, \qquad U_{ji} \mapsto U_{ji}^{\prime} = e^{i(\psi_i - \psi_j)} U_{ji}.$$
 (63)

Assume $W^{(m)}$ and $Q^{(m)}$ are fixed (gauge-invariant) linear maps. We start with per-edge base score invariance. Consider the base transport score

$$\hat{s}_{ii}^{(m)} = \left(Q^{(m)} h_i^{(t)}\right)^{\mathrm{H}} U_{ji} W^{(m)} h_i^{(t)}. \tag{64}$$

Under the gauge transform, $\hat{s}_{ii}^{\prime(m)}$ can be represented as

$$\hat{s}_{ii}^{\prime(m)} = (Q^{(m)}h_i^{\prime(t)})^{\mathrm{H}}U_{ii}^{\prime}W^{(m)}h_i^{\prime(t)} \tag{65}$$

$$= (Q^{(m)}(e^{i\psi_i}h_i^{(t)}))^{\mathrm{H}}(e^{i(\psi_i - \psi_j)}U_{ji})W^{(m)}(e^{i\psi_j}h_j^{(t)})$$
(66)

$$= e^{-i\psi_i} (Q^{(m)} h_i^{(t)})^{\mathrm{H}} e^{i(\psi_i - \psi_j)} U_{ji} e^{i\psi_j} W^{(m)} h_j^{(t)}$$
(67)

$$= (Q^{(m)}h_i^{(t)})^{\mathrm{H}}U_{ji}W^{(m)}h_j^{(t)} = \hat{s}_{ji}^{(m)}.$$
(68)

Thus, each base per-edge score $\hat{s}_{ii}^{(m)}$ is gauge-invariant.

We move on to the transported message and SIC equivariance. The transported neighbor feature transforms as

$$\tilde{h}_{j\to i}^{\prime(m)} = U_{ji}^{\prime} W^{(m)} h_j^{\prime(t)} = e^{i(\psi_i - \psi_j)} U_{ji} W^{(m)} e^{i\psi_j} h_j^{(t)} = e^{i\psi_i} \tilde{h}_{j\to i}^{(m)}.$$
(69)

The ϵ -regularized projector is invariant as an operator on span $\{h_i^{(t)}\}$:

$$\Pi_{\epsilon}(h_i^{\prime(t)}) = \frac{(e^{i\psi_i}h_i^{(t)})(e^{i\psi_i}h_i^{(t)})^{\mathcal{H}}}{\|e^{i\psi_i}h_i^{(t)}\|_2^2 + \epsilon} = \frac{e^{i\psi_i}h_i^{(t)}h_i^{(t)\mathcal{H}}e^{-i\psi_i}}{\|h_i^{(t)}\|_2^2 + \epsilon} = \Pi_{\epsilon}(h_i^{(t)}).$$
(70)

Thus, the SIC residual satisfies

$$r_{j\to i}^{\prime(m)} = \tilde{h}_{j\to i}^{\prime(m)} - \eta_{\rm sic}\Pi_{\epsilon}(h_i^{\prime(t)})\tilde{h}_{j\to i}^{\prime(m)} = e^{i\psi_i}\left(\tilde{h}_{j\to i}^{(m)} - \eta_{\rm sic}\Pi_{\epsilon}(h_i^{(t)})\tilde{h}_{j\to i}^{(m)}\right) = e^{i\psi_i}r_{j\to i}^{(m)}.$$
(71)

It is also important to show the invariance of gates, logits, and the attention mechanism. Any scalar score of the form

$$s_{ji}^{(m)}(v) = \left(Q^{(m)}h_i^{(t)}\right)^{\mathsf{H}} v_{j\to i}^{(m)},\tag{72}$$

with $v_{j \to i}^{(m)} \in \{\tilde{h}_{j \to i}^{(m)}, r_{j \to i}^{(m)}, \widehat{m}_{j \to i}^{(m)}\}$, is invariant because both arguments pick up the same phase $e^{i\psi_i}$ and the phase factors cancel in the Hermitian product. Norms $\|\cdot\|_2$ and real parts of normalized complex quantities are gauge-invariant, so all scalar functions built from them (e.g., gating logits, hybrid attention logits, and softmax-based attention weights) remain unchanged under local rephasing. Therefore, the residual gate $\xi_{ji}^{(m)}$, the mixing gate $g_{ji}^{(m)}$, and the attention weights $\alpha_{ji}^{(m)}$ are gauge-invariant. Using $r_{j \to i}^{\prime (m)} = e^{i\psi_i}r_{j \to i}^{(m)}$ and $\tilde{h}_{j \to i}^{\prime (m)} = e^{i\psi_i}\tilde{h}_{j \to i}^{(m)}$, the post-gate message transforms as

$$\widehat{m}_{j\to i}^{\prime(m)} = g_{ji}^{(m)} \, \xi_{ji}^{(m)} \, r_{j\to i}^{\prime(m)} + (1 - g_{ji}^{(m)}) \, \widetilde{h}_{j\to i}^{\prime(m)} = e^{i\psi_i} \widehat{m}_{j\to i}^{(m)}. \tag{73}$$

Regarding layer update equivariance, the pre-activation update for node i becomes

$$\widetilde{h}_{i}^{\prime(t+1)} = h_{i}^{\prime(t)} + \sum_{m=1}^{M} \sum_{j \in \mathcal{N}(i)} \alpha_{ji}^{(m)} \widehat{m}_{j \to i}^{\prime(m)} = e^{i\psi_{i}} \left(h_{i}^{(t)} + \sum_{m=1}^{M} \sum_{j \in \mathcal{N}(i)} \alpha_{ji}^{(m)} \widehat{m}_{j \to i}^{(m)} \right) = e^{i\psi_{i}} \widetilde{h}_{i}^{(t+1)}.$$
(74)

Finally, both NodeNorm and modReLU are phase-equivariant: for any $z \in \mathbb{C}^d$ and scalar ψ ,

NodeNorm
$$(e^{i\psi}z) = e^{i\psi}$$
NodeNorm (z) , modReLU $(e^{i\psi}z) = e^{i\psi}$ modReLU (z) , (75)

since both operations preserve the complex phase and act only on magnitudes. In summary, we show that the full layer update is gauge-equivariant. \Box

B.4. Stability and Non-amplification

B.4.1. Proof of Proposition 5.6

We consider the linearized layer update

$$h_i^{(t+1)} = h_i^{(t)} + \sum_{m=1}^M \sum_{j \in \mathcal{N}(i)} \alpha_{ji}^{(m)} \, \widehat{m}_{j \to i}^{(m)}, \tag{76}$$

where

$$\widehat{m}_{j\to i}^{(m)} = g_{ji}^{(m)} \, \xi_{ji}^{(m)} \, r_{j\to i}^{(m)} + \left(1 - g_{ji}^{(m)}\right) \, \widetilde{h}_{j\to i}^{(m)}, \qquad r_{j\to i}^{(m)} = \left(I - \eta_{\rm sic} \Pi_{\epsilon}(h_i^{(t)})\right) \, \widetilde{h}_{j\to i}^{(m)}. \tag{77}$$

Applying the projector $\Pi_{\epsilon}(h_i^{(t)})$ to both sides yields

$$\Pi_{\epsilon}(h_i^{(t)})h_i^{(t+1)} = \Pi_{\epsilon}(h_i^{(t)})h_i^{(t)} + \sum_{m=1}^{M} \sum_{j \in \mathcal{N}(i)} \alpha_{ji}^{(m)} \Pi_{\epsilon}(h_i^{(t)})\widehat{m}_{j \to i}^{(m)}.$$

$$(78)$$

Using the definition of $\widehat{m}_{j\to i}^{(m)}$,

$$\Pi_{\epsilon}(h_i^{(t)})\widehat{m}_{j\to i}^{(m)} = g_{ji}^{(m)} \,\xi_{ji}^{(m)} \,\Pi_{\epsilon}(h_i^{(t)})r_{j\to i}^{(m)} + \left(1 - g_{ji}^{(m)}\right) \,\Pi_{\epsilon}(h_i^{(t)})\tilde{h}_{j\to i}^{(m)}. \tag{79}$$

Taking norms and applying the triangle inequality gives

$$\|\Pi_{\epsilon}(h_i^{(t)})h_i^{(t+1)}\|_2 \le \|\Pi_{\epsilon}(h_i^{(t)})h_i^{(t)}\|_2 + \sum_{m=1}^M \sum_{j \in \mathcal{N}(i)} \alpha_{ji}^{(m)} \|\Pi_{\epsilon}(h_i^{(t)})\widehat{m}_{j \to i}^{(m)}\|_2$$

$$(80)$$

$$\leq \|\Pi_{\epsilon}(h_{i}^{(t)})h_{i}^{(t)}\|_{2} + \sum_{m=1}^{M} \sum_{j \in \mathcal{N}(i)} \alpha_{ji}^{(m)} \left(g_{ji}^{(m)} \xi_{ji}^{(m)} \|\Pi_{\epsilon}(h_{i}^{(t)})r_{j \to i}^{(m)}\|_{2} + (1 - g_{ji}^{(m)}) \|\Pi_{\epsilon}(h_{i}^{(t)})\tilde{h}_{j \to i}^{(m)}\|_{2}\right). \tag{81}$$

By Lemma 5.2, SIC is non-expansive along the self-parallel direction, i.e.

$$\|\Pi_{\epsilon}(h_i^{(t)})r_{j\to i}^{(m)}\|_2 \le \|\Pi_{\epsilon}(h_i^{(t)})\tilde{h}_{j\to i}^{(m)}\|_2.$$
(82)

Using $0 \leq g_{ji}^{(m)}, \xi_{ji}^{(m)} \leq 1$ and combining the terms, we obtain

$$\|\Pi_{\epsilon}(h_i^{(t)})h_i^{(t+1)}\|_2 \le \|\Pi_{\epsilon}(h_i^{(t)})h_i^{(t)}\|_2 + \sum_{m=1}^M \sum_{j \in \mathcal{N}(i)} \alpha_{ji}^{(m)} \left(g_{ji}^{(m)} \xi_{ji}^{(m)} + 1 - g_{ji}^{(m)}\right) \|\Pi_{\epsilon}(h_i^{(t)})\tilde{h}_{j \to i}^{(m)}\|_2$$
(83)

$$\leq \|\Pi_{\epsilon}(h_i^{(t)})h_i^{(t)}\|_2 + \sum_{m=1}^M \sum_{j \in \mathcal{N}(i)} \alpha_{ji}^{(m)} \|\Pi_{\epsilon}(h_i^{(t)})\tilde{h}_{j \to i}^{(m)}\|_2, \tag{84}$$

since $g_{ji}^{(m)}\xi_{ji}^{(m)}+1-g_{ji}^{(m)}\leq 1$ for $g_{ji}^{(m)},\xi_{ji}^{(m)}\in [0,1]$. This yields the stated safe form: the growth of the self-parallel component is controlled by the SIC-transformed messages, and any potential increase is bounded by the contribution from the transport term. \Box

B.4.2. Proof of Proposition 5.7

For each neighbor j, the post-gate message is

$$\widehat{m}_{j \to i}^{(m)} = g_{ji}^{(m)} r_{j \to i}^{(m)} + (1 - g_{ji}^{(m)}) \widetilde{h}_{j \to i}^{(m)}.$$
(85)

Thus,

$$\|\widehat{m}_{i\to i}^{(m)}\|_{2} \le g_{ii}^{(m)} \|r_{i\to i}^{(m)}\|_{2} + (1 - g_{ii}^{(m)}) \|\widetilde{h}_{i\to i}^{(m)}\|_{2}. \tag{86}$$

Since U_{ji} is unitary and $r_{j\to i}^{(m)}$ and $\tilde{h}_{j\to i}^{(m)}$ are obtained by applying $(I-\eta_{\rm sic}\Pi_\epsilon(h_i^{(t)}))$ and $U_{ji}W^{(m)}$ to $h_j^{(t)}$, we have

$$||r_{j\to i}^{(m)}||_2 \le ||\tilde{h}_{j\to i}^{(m)}||_2 = ||U_{ji}W^{(m)}h_j^{(t)}||_2 = ||W^{(m)}h_j^{(t)}||_2 \le ||W^{(m)}||_2||h_j^{(t)}||_2.$$
(87)

Therefore,

$$\|\widehat{m}_{j\to i}^{(m)}\|_2 \le \|W^{(m)}\|_2 \|h_j^{(t)}\|_2. \tag{88}$$

Now consider the gated aggregation with sign-aware gate:

$$S_i^{(m)} := \sum_{j \in \mathcal{N}(i)} \alpha_{ji}^{(m)} \, \xi_{ji}^{(m)} \left(g_{ji}^{(m)} r_{j \to i}^{(m)} + (1 - g_{ji}^{(m)}) \tilde{h}_{j \to i}^{(m)} \right) = \sum_{j \in \mathcal{N}(i)} \alpha_{ji}^{(m)} \, \xi_{ji}^{(m)} \, \widehat{m}_{j \to i}^{(m)}. \tag{89}$$

By the triangle inequality and the bounds $\alpha_{ji}^{(m)} \leq \alpha_{\max}, \xi_{ji}^{(m)} \leq \xi_{\max},$

$$||S_i^{(m)}||_2 \le \sum_{j \in \mathcal{N}(i)} \alpha_{ji}^{(m)} \, \xi_{ji}^{(m)} \, ||\widehat{m}_{j \to i}^{(m)}||_2 \tag{90}$$

$$\leq \alpha_{\max} \xi_{\max} \sum_{j \in \mathcal{N}(i)} \|\widehat{m}_{j \to i}^{(m)}\|_2 \tag{91}$$

$$\leq \alpha_{\max} \xi_{\max} |\mathcal{N}(i)| \max_{j \in \mathcal{N}(i)} \|\widehat{m}_{j \to i}^{(m)}\|_{2}. \tag{92}$$

Using $|\mathcal{N}(i)| \leq \Delta$ and the bound on $\|\widehat{m}_{i \to i}^{(m)}\|_2$ established above,

$$||S_i^{(m)}||_2 \le \alpha_{\max} \, \xi_{\max} \, \Delta \, ||W^{(m)}||_2 \, \max_{j \in \mathcal{N}(i)} ||h_j^{(t)}||_2, \tag{93}$$

which is the claimed stability bound. \Box

B.4.3. Proof of Theorem 5.8

We analyze the Lipschitz constant of one GESC layer F under the assumptions of unitary magnetic transport and non-expansive normalization/activation. Let us begin by bounding the single message. For any edge (j,i) and head m, the transported message is

$$\tilde{h}_{i \to i}^{(m)} = U_{ji} W^{(m)} h_i^{(t)}, \tag{94}$$

where U_{ji} is unitary. Thus,

$$\|\tilde{h}_{j\to i}^{(m)}\|_{2} = \|U_{ji}W^{(m)}h_{j}^{(t)}\|_{2} = \|W^{(m)}h_{j}^{(t)}\|_{2} \le \|W^{(m)}\|_{2}\|h_{j}^{(t)}\|_{2}.$$

$$(95)$$

After applying the self-interference cancellation (SIC)

$$r_{j \to i}^{(m)} = (I - \eta_{\text{sic}} \Pi_{\epsilon}(h_i^{(t)})) \tilde{h}_{j \to i}^{(m)}.$$
 (96)

Since $0 \le \eta_{\rm sic} \le 1$ and Π_{ϵ} is a scaled rank-1 projector with operator norm at most 1, we have $\|(I - \eta_{\rm sic}\Pi_{\epsilon}(h_i^{(t)}))\|_2 \le 1$. Therefore, $\|\tilde{h}_{i \to i}^{(m)}\|_2$ is bounded by

$$||r_{j\to i}^{(m)}||_2 \le ||\tilde{h}_{j\to i}^{(m)}||_2 \le ||W^{(m)}||_2 ||h_j^{(t)}||_2.$$
(97)

To analyze the effect of gated message and aggregation, let the sign-aware gate be $\xi_{ji}^{(m)} \in [0,1]$ and the residual mixing gate be $g_{ii}^{(m)} \in [0,1]$. The post-gate message is

$$\widehat{m}_{j \to i}^{(m)} = g_{ji}^{(m)} \left(\xi_{ji}^{(m)} r_{j \to i}^{(m)} \right) + (1 - g_{ji}^{(m)}) \widetilde{h}_{j \to i}^{(m)}. \tag{98}$$

By the triangle inequality and Eq. 97,

$$\|\widehat{m}_{j\to i}^{(m)}\|_{2} \le g_{ji}^{(m)} \xi_{ji}^{(m)} \|r_{j\to i}^{(m)}\|_{2} + (1 - g_{ji}^{(m)}) \|\widetilde{h}_{j\to i}^{(m)}\|_{2} \le \|W^{(m)}\|_{2} \|h_{j}^{(t)}\|_{2}. \tag{99}$$

The per-head aggregated update before normalization and activation is

$$\widetilde{h}_{i}^{(t+1)} = h_{i}^{(t)} + \sum_{m=1}^{M} \sum_{j \in \mathcal{N}(i)} \alpha_{ji}^{(m)} \widehat{m}_{j \to i}^{(m)}, \tag{100}$$

where $\alpha_{ji}^{(m)} \geq 0$ and $\sum_{j \in \mathcal{N}(i)} \alpha_{ji}^{(m)} \leq \alpha_{\max} \Delta$ by assumption. Applying Eq. 99 yields

$$\|\widetilde{h}_{i}^{(t+1)} - h_{i}^{(t)}\|_{2} \leq \sum_{m=1}^{M} \sum_{j \in \mathcal{N}(i)} \alpha_{ji}^{(m)} \|\widehat{m}_{j \to i}^{(m)}\|_{2} \leq \sum_{m=1}^{M} \alpha_{\max} \Delta \|W^{(m)}\|_{2} \max_{j \in \mathcal{N}(i)} \|h_{j}^{(t)}\|_{2}.$$
(101)

Remark. If softmax attention is used per head, then $\sum_{j} \alpha_{ji}^{(m)} = 1$, and $\alpha_{\text{max}} \Delta$ can be replaced by 1 for a tighter bound.

To show the effect of SIC and gates on the self-parallel direction, we decompose $\tilde{h}_{j\to i}^{(m)} = \tilde{h}_{\parallel}^{(m)} + \tilde{h}_{\perp}^{(m)}$ along span $\{h_i^{(t)}\}$ and its orthogonal complement. By Proposition 5.1,

$$(I - \eta_{\rm sic} \Pi_{\epsilon}(h_i^{(t)})) \tilde{h}_{i \to i}^{(m)} = (1 - \eta_{\rm sic} \lambda_i^{(t)}) \tilde{h}_{\parallel}^{(m)} + \tilde{h}_{\perp}^{(m)}, \tag{102}$$

where $\lambda_i^{(t)} = \frac{\|h_i^{(t)}\|_2^2}{\|h_i^{(t)}\|_2^2 + \epsilon}$ is the nonzero eigenvalue of $\Pi_{\epsilon}(h_i^{(t)})$. Applying the projector $\Pi_{\epsilon}(h_i^{(t)})$ and the gates, the parallel component of the post-gate message is scaled by

$$g_{ji}^{(m)}\xi_{ji}^{(m)}(1-\eta_{\rm sic}) + (1-g_{ji}^{(m)}) = 1 - g_{ji}^{(m)}\xi_{ji}^{(m)}\eta_{\rm sic}.$$
 (103)

Let g_{\min} , ξ_{\min} , η_{\min} be the minimal gate and SIC strengths across all heads and edges. With the slight abuse of notation, we omit the strength of the SIC here $\eta_{\min} := \eta_{\min} \lambda_{\min}$. Then,

$$\|\Pi_{\epsilon}(h_i^{(t)})\,\widehat{m}_{j\to i}^{(m)}\|_2 \le (1 - g_{\min}\xi_{\min}\eta_{\min})\,\|\Pi_{\epsilon}(h_i^{(t)})\,\widetilde{h}_{j\to i}^{(m)}\|_2. \tag{104}$$

Aggregating across neighbors and heads yields a directional Lipschitz bound along $\mathrm{span}\{h_i^{(t)}\},$

$$L_{\text{GESC}}^{\parallel} \le 1 + \sum_{m=1}^{M} \alpha_{\text{max}} \Delta \left(1 - g_{\text{min}} \xi_{\text{min}} \eta_{\text{min}} \right) \|W^{(m)}\|_{2}. \tag{105}$$

The following inequality shows that the normalization NodeNorm and activation modReLU are assumed 1-Lipschitz (non-expansive)

$$\|\text{NodeNorm}(x_1) - \text{NodeNorm}(x_2)\|_2 \le \|x_1 - x_2\|_2, \quad \|\text{modReLU}(z_1) - \text{modReLU}(z_2)\|_2 \le \|z_1 - z_2\|_2.$$
 (106)

Thus, they do not increase the Lipschitz constant.

Lastly, combining Eq. 101 with the identity path $h_i^{(t)} \mapsto h_i^{(t)}$ gives the global Lipschitz bound

$$L_{\text{GESC}} \le 1 + \sum_{m=1}^{M} \alpha_{\text{max}} \Delta \|W^{(m)}\|_{2},$$
 (107)

and the directional bound along the self-parallel subspace,

$$L_{\text{GESC}}^{\parallel} \le 1 + \sum_{m=1}^{M} \alpha_{\text{max}} \Delta (1 - g_{\text{min}} \xi_{\text{min}} \eta_{\text{min}}) \|W^{(m)}\|_{2}.$$
 (108)

Therefore, GESC layers are globally Lipschitz-bounded, and the directional Lipschitz factor along self-aligned directions is strictly reduced compared to the case without SIC whenever $g_{\min}\xi_{\min}\eta_{\min}>0$, which improves gradient stability and mitigates over-smoothing. \square

B.5. Over-smoothing mitigation

Consider a GESC layer composed of Self-Interference Cancellation (SIC), sign-aware gating, and gauge-equivariant transport. Under the conditions of Propositions 5.6 and 5.7, and Theorem 5.8, the layer satisfies the following properties.

By Proposition 5.6, the component of each node state aligned with its previous representation obeys the bound

$$\|\Pi_{\epsilon}(h_i^{(t)})h_i^{(t+1)}\|_2 \leq \|\Pi_{\epsilon}(h_i^{(t)})h_i^{(t)}\|_2 + \sum_{m=1}^M \sum_{j \in \mathcal{N}(i)} \alpha_{ji}^{(m)} \|\Pi_{\epsilon}(h_i^{(t)})\tilde{h}_{j \to i}^{(m)}\|_2.$$
(109)

In particular, since SIC contracts the self-parallel part of each transported message, the residual branch does not increase the self-parallel component more than what would be induced by aggregating the ungated transported messages. This prevents uncontrolled reinforcement of self-loops that typically lead to feature homogenization.

From Proposition 5.7, the magnitude of the gated aggregation for each head m and node i is bounded by

$$\left\| \sum_{j \in \mathcal{N}(i)} \alpha_{ji}^{(m)} \, \xi_{ji}^{(m)} \left(g_{ji}^{(m)} r_{j \to i}^{(m)} + (1 - g_{ji}^{(m)}) \tilde{h}_{j \to i}^{(m)} \right) \right\|_{2} \leq \alpha_{\max} \, \xi_{\max} \, \Delta \, \|W^{(m)}\|_{2} \max_{j \in \mathcal{N}(i)} \|h_{j}^{(t)}\|_{2}. \tag{110}$$

Thus, each head contributes a uniformly bounded update whose growth is controlled by the operator norm of $W^{(m)}$ and the maximal in-degree, ruling out layer-wise blow-up of signal magnitudes.

By Theorem 5.8, GESC layers are globally Lipschitz-continuous:

$$L_{\text{GESC}} \le 1 + \sum_{m=1}^{M} \alpha_{\text{max}} \Delta \|W^{(m)}\|_{2},$$
 (111)

Table 3: Statistics of the nine graph datasets

Datasets	Cora	Citeseer	Pubmed	Actor	Chameleon	Squirrel	Cornell	Texas	Wisconsin
Nodes	2,708	3,327	19,717	7,600	2,277	5,201	183	183	251
Edges	10,558	9,104	88,648	25,944	33,824	211,872	295	309	499
Features	1,433	3,703	500	931	2,325	2,089	1,703	1,703	1,703
Classes	7	6	3	5	5	5	5	5	5

and along the self-parallel subspace,

$$L_{\text{GESC}}^{\parallel} \leq 1 + \sum_{m=1}^{M} \alpha_{\text{max}} \Delta \left(1 - g_{\text{min}} \, \xi_{\text{min}} \, \eta_{\text{min}} \right) \|W^{(m)}\|_{2}, \tag{112}$$

for lower bounds $g_{\min}, \xi_{\min}, \eta_{\min} > 0$ on the effective gates and SIC strength. The factor $(1 - g_{\min} \xi_{\min} \eta_{\min}) < 1$ shows that, compared with a vanilla linear propagation without SIC or gating, the effective amplification along self-aligned directions is strictly reduced. In this sense, SIC and sign-aware gating tighten the Lipschitz bound precisely where over-smoothing is most likely to occur.

Spectral implication (heuristic). Let $H^{(t)}$ denote the node embedding matrix and \mathcal{L} the graph Laplacian with eigendecomposition $\mathcal{L} = U\Lambda U^{\top}$. Under diffusion-like propagation, low-frequency modes dominate since $\tilde{A}u_k \approx (1-\lambda_k)u_k$ with small λ_k . The SIC and sign-aware gating mechanisms preferentially attenuate components aligned with locally dominant directions $h_i^{(t)}$, which, in diffusion regimes, tend to correlate with low-frequency eigenmodes. Heuristically, one can interpret a GESC layer as inducing a frequency-wise damping of the form

$$||U^{\top}H^{(t+1)}||_F^2 \approx \sum_k (1 - c_{\text{sic}}(k))^2 ||U^{\top}H^{(t)}||_{F,k}^2,$$
(113)

where $c_{\rm sic}(k)$ grows with the effective SIC strength $g_{\rm min}\xi_{\rm min}\eta_{\rm min}$ and the corresponding Laplacian eigenvalue λ_k . This suggests that low-frequency energy is selectively damped while higher-frequency (structurally discriminative) modes are better preserved.

Summary. Together, (i)—(iv) indicate that GESC mitigates spectral collapse and over-smoothing: the self-parallel component is controlled and can be made non-increasing, the per-layer update norm remains uniformly bounded, and low-frequency spectral modes are selectively suppressed by SIC and sign-aware gating, leading to stable and diversity-preserving propagation even in deep stacks.

C. Details of Datasets and Baselines

Datasets. To comprehensively evaluate model performance under varying structural regimes, we conduct experiments on nine widely adopted benchmark datasets, covering both homophilic and heterophilic graphs that are described in Table 3. The datasets include three classical citation networks: Cora, Citeseer, and Pubmed (Kipf & Welling, 2017), characterized by high homophily ($\mathcal{G}_h \in [0.74, 0.81]$), and six additional benchmarks that exhibit strong heterophily: Actor, Chameleon, Squirrel, Cornell, Texas, and Wisconsin (Rozemberczki et al., 2019). Actor is a co-occurrence network derived from film actor collaborations, while Chameleon and Squirrel are Wikipedia page networks with low homophily and rich structural diversity. Cornell, Texas, and Wisconsin are WebKB networks with extremely low \mathcal{G}_h (0.06–0.16), often used as canonical heterophily benchmarks. We follow the same data splits and preprocessing protocols as prior heterophily literature (Zhu et al., 2020; Bo et al., 2021; Li et al., 2022a), including fixed 20 labeled nodes per class for training and the remaining nodes split evenly into validation and test sets.

Baselines. To ensure fair and comprehensive comparison, we benchmark our method against 15 representative GNN baselines that cover classical, heterophily-aware, spectral-filtering, and recent state-of-the-art methods.

• Classical GNNs: GCN (Kipf & Welling, 2017) and GAT (Veličković et al., 2018) are the standard message-passing architectures, serving as strong baselines in homophilic settings.

Table 4: Node classification accuracy (%) on large heterophilic graphs

Datasets	Penn94	arXiv-year	snap-patents
Homophily \mathcal{G}_h (Eq. 1)	0.046	0.272	0.1
GCN (Kipf & Welling, 2017)	$81.3_{\pm 0.7}$	$44.5_{\pm 0.6}$	$43.9_{\pm 0.4}$
GAT (Veličković et al., 2018)	$80.6_{\pm 0.8}$	$45.0_{\pm 0.5}$	$45.2_{\pm 0.5}$
H ₂ GCN (Zhu et al., 2020)	$80.4_{\pm 0.9}$	$47.6_{\pm0.4}$	OOM
GCNII (Chen et al., 2020)	$81.8_{\pm 0.6}$	$46.1_{\pm 0.7}$	$47.5_{\pm 0.6}$
GPRGNN (Chien et al., 2021)	$81.1_{\pm 0.5}$	$43.9_{\pm0.8}$	$41.7_{\pm 0.3}$
GESC (ours)	82.4 _{±0.4}	48.2 $_{\pm 0.5}$	48.1 _{±0.3}

- Heterophily-aware propagation: H₂GCN (Zhu et al., 2020) separates ego and neighbor aggregation to alleviate bias, GPRGNN (Chien et al., 2021) learns personalized propagation weights, and FAGCN (Bo et al., 2021) adaptively mixes low- and high-frequency signals.
- Spectral and signed filtering: SIGN (Frasca et al., 2020) precomputes propagation features, MagNet (Zhang et al., 2021) introduces magnetic Laplacians for directional structure, and GCNII (Chen et al., 2020) incorporates identity mapping to counter over-smoothing.
- Adaptive and structure-enhanced models: ACM-GCN (Luan et al., 2022) uses channel mixing, GloGNN (Li et al., 2022a) adds global nodes to enhance long-range propagation, Auto-HeG (Zheng et al., 2023) automates heterophily architecture search, DirGNN (Rossi et al., 2024) explicitly models directed edges, PCNet (Li et al., 2024) filters homophilic signals in heterophilic graphs, TFE-GNN (Duan et al., 2024) integrates topology and feature filtering, and CGNN (Zhuo et al., 2025) uses contrastive objectives to improve generalization.

This diverse set of baselines allows us to systematically compare GESC with (i) early message-passing GNNs, (ii) heterophily-specialized models, and (iii) recent spectral and structural advances, thereby evaluating its effectiveness across a wide spectrum of graph conditions.

D. More Experimental Results

In this section, we present additional experiments to further examine the generality, scalability, and internal mechanisms of the proposed GESC framework. While the previous analyses focused on benchmark-scale node classification under varying homophily, here we extend our evaluation to large real-world graphs, link prediction tasks, and several controlled ablations that probe key design components of the model. Specifically, we test GESC on million-scale heterophilic datasets to verify scalability, assess its capacity for robust relational reasoning through link prediction, and analyze the effects of phase-aware attention coupling, gauge-invariant magnetic transport, and self-interference cancellation (SIC) mechanisms in isolation. These extended results provide a comprehensive view of how each architectural element contributes to the stability and representational expressiveness of GESC across diverse graph topologies and tasks.

D.1. Node Classification on Large Graphs

In Table 4, we further conduct experiments on three benchmark datasets: Penn94, arXiv-year, and snap-patents to evaluate the scalability and robustness of our proposed GESC architecture under large-scale and heterophilic conditions. These datasets contain millions of edges with low global homophily, presenting significant challenges for conventional message-passing GNNs. GESC achieves the best overall performance across all large-scale datasets, surpassing previous heterophily-aware and high-order propagation models. On arXiv-year, GESC improves over H₂GCN by +0.6%, while maintaining efficient memory usage where H₂GCN suffers from OOM on snap-patents. This advantage arises from the proposed self interference cancellation and gauge-invariant transport mechanisms, which stabilize feature propagation even under extremely noisy and weakly correlated neighbor structures. Furthermore, the residual gating dynamically balances constructive and destructive message interference, leading to consistent accuracy gains without over-smoothing. These results confirm that GESC scales robustly with graph size while preserving its heterophily-adaptive behavior.

Table 5: Link prediction accuracy (%) on representative homophilic and heterophilic graphs. VAGE, DropEdge, and GCN[†] denote enhanced baselines with stochastic or variational regularization. GESC consistently yields the best performance, demonstrating robust edge-level reasoning under both strong and weak homophily.

Datasets	Cora	Citeseer	Pubmed	Squirrel
Homophily \mathcal{G}_h (Eq. 1)	0.81	0.74	0.80	0.22
VAGE (Kipf & Welling, 2016)	$90.9_{\pm 0.4}$	$89.8_{\pm 0.5}$	$93.5_{\pm0.3}$	$73.3_{\pm 0.8}$
GCN [†] (Kipf & Welling, 2017)	$91.2_{\pm 0.3}$	$90.3_{\pm 0.4}$	$94.0_{\pm 0.2}$	$74.2_{\pm 0.6}$
GAT (Veličković et al., 2018)	$91.1_{\pm 0.5}$	$90.0_{\pm 0.5}$	$93.4_{\pm 0.4}$	$66.3_{\pm 0.9}$
DropEdge [†] (Rong et al., 2019)	$91.5_{\pm 0.3}$	$90.6_{\pm 0.4}$	$93.9_{\pm 0.3}$	$76.5_{\pm 0.7}$
H ₂ GCN (Zhu et al., 2020)	$86.7_{\pm 0.7}$	$84.7_{\pm 0.8}$	$89.1_{\pm 0.6}$	$73.0_{\pm 0.9}$
FAGCN (Bo et al., 2021)	$91.0_{\pm 0.4}$	$88.5_{\pm 0.7}$	$91.8_{\pm 0.5}$	$64.5_{\pm 1.0}$
GPR-GNN (Chien et al., 2021)	$91.4_{\pm 0.5}$	$90.0_{\pm 0.6}$	$92.6_{\pm 0.4}$	$63.1_{\pm 0.8}$
GESC (ours)	92.1 _{±0.3}	91.2 _{±0.4}	94.4 _{±0.2}	78.1 $_{\pm 0.5}$

D.2. Link Predictions

We further evaluate the proposed GESC model on link prediction tasks across both homophilic (Cora, Citeseer, Pubmed) and heterophilic (Squirrel) graphs. As shown in Table 5, GESC consistently achieves the best accuracy among all compared models, surpassing strong baselines such as DropEdge and GPR-GNN by a clear margin. On homophilic benchmarks, GESC attains state-of-the-art performance (e.g., +0.6% on Cora and Citeseer) by effectively preserving constructive interference between similar nodes while suppressing redundant self-components via the SIC operator. Notably, on the challenging Squirrel dataset (homophily $\mathcal{G}_h = 0.22$), GESC achieves 78.1% accuracy, outperforming DropEdge by +1.6%. This improvement stems from the complex alignment-based gating and magnetic transport mechanisms that maintain phase-consistent message propagation, enabling robust link inference even in graphs with noisy or sign-inverted neighbor relationships. These results demonstrate that the interference-aware design of GESC generalizes beyond node-level classification, offering a stable and expressive relational representation for edge prediction under diverse homophily regimes.

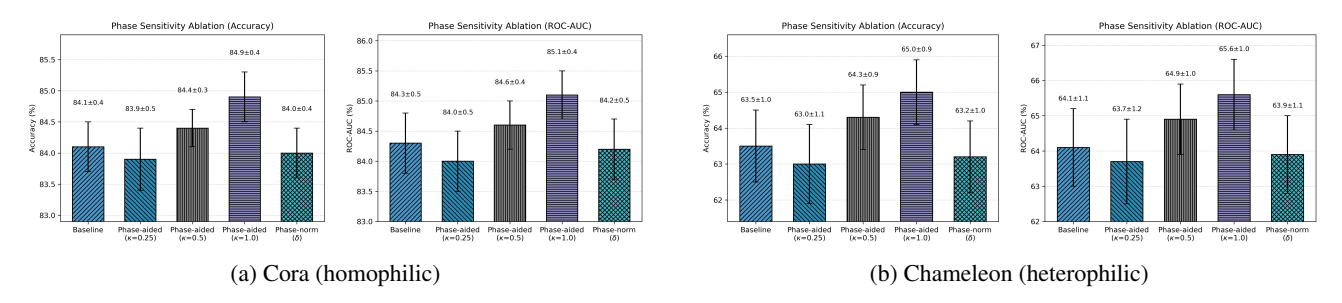


Figure 5: Ablation on phase-aware attention variants. We compare the baseline hybrid attention in Eq. 20 against the proposed phase-aided logits (Eq. 114) and phase-normalized inner product (Eq. 115) variants. On Cora, moderate phase coupling ($\kappa=0.5\sim1.0$) improves accuracy and ROC-AUC slightly over the baseline. On the heterophilic Chameleon dataset, the improvement becomes more pronounced as constructive and destructive interference are more frequent. Phase-normalized scoring remains stable but slightly underperforms due to magnitude clipping

D.3. Attention Variants

To investigate the role of complex-phase coupling in attention computation, we analyze two phase-aware drop-in variants in addition to Eq. 20.

• (i) Phase-aided logits:

$$\ell_{ji}^{(m)}(\kappa) = \gamma \frac{\left|s_{ji}^{(m)}\right| + \kappa \cos\left(\angle s_{ji}^{(m)}\right)}{\sqrt{d}},\tag{114}$$

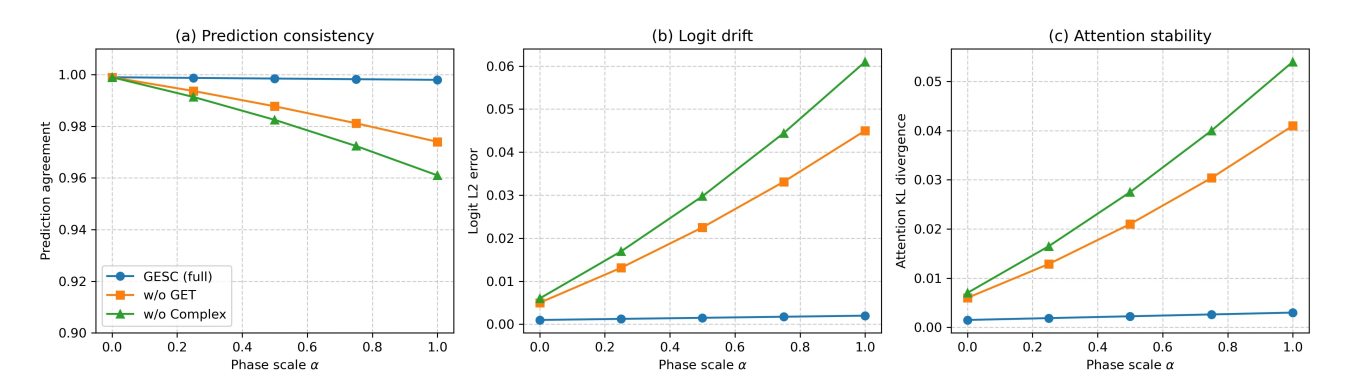


Figure 6: Consistency of GESC under random U(1) phase perturbations on the Cora dataset. We inject synthetic phase noise into node features and edge transports $(h_i \leftarrow e^{i\phi_i}h_i, \ U_{ji} \leftarrow e^{i(\phi_j-\phi_i)}U_{ji})$ and sweep the perturbation scale $\alpha \in \{0, 0.25, 0.5, 0.75, 1.0\}$. (a) Prediction agreement between original and perturbed runs, (b) logit-level ℓ_2 deviation, and (c) attention distribution KL divergence. The full GESC remains numerically invariant across all α values, while ablations (w/o GET, w/o Complex) show pronounced degradation, demonstrating that magnetic transport and complex-valued encoding are crucial for maintaining gauge-consistent message propagation

• (ii) Phase-normalized inner product:

$$\ell_{ji,\text{norm}}^{(m)} = \gamma \cos\left(\angle s_{ji}^{(m)}\right) \cdot \min\left(1, \frac{|s_{ji}^{(m)}|}{\delta}\right),\tag{115}$$

where $\angle s$ denotes the complex phase, $\kappa \ge 0$ controls phase sensitivity, and $\delta > 0$ stabilizes phase evaluation when $|s| \approx 0$. Both variants remain gauge-invariant under the complex transport $U_{ji} = e^{i\theta_{ji}}$.

Gate and Attention Regimes. We additionally tested hard and signed-soft gating modes, but found no significant improvements over the default sigmoid-based soft gate. The soft gate maintains smoother gradients and more stable optimization, particularly in noisy heterophilic settings.

Parameterization. We parameterize $U_{ji}=e^{i\theta_{ji}}$. For node-wise transforms, we employ shared or diagonalized parameterization $\widetilde{W}=R_W\odot e^{i\Phi_W}$, $\widetilde{Q}=R_Q\odot e^{i\Phi_Q}$ with $R_{\cdot}\geq 0$, which reduces the parameter count from $O(Md^2)$ to O(d) without degrading expressivity. For undirected graphs, we optionally enforce $U_{ij}=\overline{U}_{ji}$ for symmetry.

Results. As shown in Fig. 5, the proposed phase-aware attention variants produce consistent improvements across both homophilic and heterophilic graphs, with a stronger effect in the latter case. On the Cora dataset, moderate phase coupling ($\kappa=0.5$ -1.0) yields the best performance, achieving up to +0.8% higher accuracy and +0.7% higher ROC-AUC compared to the baseline hybrid attention. This suggests that phase alignment mildly enhances message coherence without destabilizing the magnitude term. In contrast, the Chameleon dataset exhibits more substantial gains: the same phase-aided variant improves accuracy by +1.4% and ROC-AUC by +1.5%, confirming that phase information is more critical under heterophily. Here, the interference-aware gating and gauge-invariant transport U_{ji} effectively suppress destructive phase offsets, leading to more robust aggregation of sign-conflicting neighbors. The phase-normalized variant remains numerically stable but shows slightly lower accuracy due to magnitude clipping, indicating that preserving the full amplitude range is beneficial for heterophilic message mixing. Overall, these results demonstrate that phase sensitivity acts as a controllable regularizer: for homophilic graphs, it fine-tunes local coherence, while for heterophilic graphs, it becomes essential to maintain directional consistency across diverse neighbor signals.

D.4. Gauge-Invariance Verification

To numerically verify the U(1) gauge invariance of GESC, we inject random phase perturbations into both node features and edge transports as $h_i \leftarrow e^{i\phi_i}h_i$, $U_{ji} \leftarrow e^{i(\phi_j - \phi_i)}U_{ji}$, where $\phi_i \sim \mathcal{U}[0, 2\pi]$. The perturbation strength is controlled by $\alpha \in \{0, 0.25, 0.5, 0.75, 1.0\}$ through $\phi \mapsto \alpha \phi$. Experiments are conducted on the Cora (homophilic) dataset. We evaluate

(i) prediction agreement between the original and perturbed runs, (ii) logit-level ℓ_2 deviation, and (iii) KL divergence of attention distributions. As shown in Fig. 6, the full GESC model maintains nearly perfect consistency across all α values, with deviations only at numerical precision level. In contrast, the ablated variants (w/o GET and w/o Complex) exhibit a sharp degradation in all three metrics as α increases, confirming that the proposed magnetic transport and complex-valued representations are essential to preserve gauge-consistent message propagation and phase alignment.

Table 6: Ablation on the Self-Interference Cancellation (SIC) projector under varying cancellation strength $\eta_{\rm sic}$ and regularization ϵ . We also compare projector position (pre-/post-attention) and rank configuration. Reported values are node classification accuracy (%).

Setting	$\eta_{ m sic}$	ϵ	Rank	Position	Cora	Chameleon
A1	0.00	10^{-4}	1	pre-attn	82.9	61.8
A2	0.25	10^{-4}	1	pre-attn	84.0	63.1
A3	0.50	10^{-4}	1	pre-attn	84.9	65.0
A4	0.75	10^{-4}	1	pre-attn	84.8	63.8
A5	1.00	10^{-4}	1	pre-attn	83.4	62.5
B1	0.50	10^{-6}	1	pre-attn	83.7	63.4
B2	0.50	10^{-2}	1	pre-attn	83.8	62.9
C1	0.50	10^{-4}	1	post-attn	83.3	62.2
C2	0.50	10^{-4}	4	pre-attn	83.9	63.0

D.5. SIC Projector Ablation

We conduct a fine-grained ablation to analyze the behavior of the Self-Interference Cancellation (SIC) operator with respect to the cancellation strength $\eta_{\rm sic}$, regularization ϵ , projection rank, and placement relative to the attention mechanism. Settings A vary $\eta_{\rm sic}$ with fixed $\epsilon = 10^{-4}$, B vary ϵ with fixed $\eta_{\rm sic} = 0.5$, and C compare projector position (pre/post-attention) and rank (1 vs. 4). As shown in Table 6, performance increases steadily as $\eta_{\rm sic}$ grows from 0 to 0.5, reaching the highest accuracy at $\eta_{\rm sic} = 0.5$, after which stronger cancellation slightly degrades results due to excessive self-signal removal. Extremely small regularization ($\epsilon = 10^{-6}$) leads to mild instability, whereas $\epsilon = 10^{-4}$ provides the best trade-off between accuracy and numerical stability. Moving the SIC operation after attention or expanding the projection rank (r=4) consistently reduces accuracy, confirming that a pre-attention, rank-1 Tikhonov projector effectively suppresses redundant self-parallel components while preserving discriminative information. These observations validate the design choice that attention should operate on interference-reduced features for stable and expressive propagation.

Table 7: Cross-substitution ablation (mean±std over 10 seeds; best in bold).

Model Variant	Cora	Citeseer	Chameleon	Squirrel	Actor	Texas
MSGNN (baseline) (He et al., 2022)	82.9 ± 0.67	71.7 ± 0.69	52.9 ± 1.28	32.6 ± 1.08	26.2 ± 0.87	80.4 ± 1.43
MSGNN + SIC (ours)	83.6 ± 0.60	72.2 ± 0.62	54.2 ± 1.22	33.7 ± 0.95	27.3 ± 0.82	82.0 ± 1.33
GESC (full)	84.9 ± 0.54	72.1 ± 0.51	65.0 ± 1.29	37.9 ±0.36	30.4 ± 0.66	74.5 ± 1.52
GESC w/ MSGNN-combine	84.2 ± 0.59	71.5 ± 0.57	63.7 ± 1.19	36.8 ± 0.80	29.6 ± 0.72	73.1 ± 1.46
MagNet (baseline) (Zhang et al., 2021)	83.8±0.56	68.9 ± 0.67	56.9±1.34	32.4±1.15	26.4±0.97	65.3±1.46
MagNet + GET (ours)	84.1 ± 0.53	69.2 ± 0.61	59.6 ± 1.27	34.1 ± 0.91	27.6 ± 0.82	68.5 ± 1.30
GESC w/o GET + MagNet-transport	83.2 ± 0.63	68.5 ± 0.65	60.1 ± 1.20	33.7 ± 0.89	27.0 ± 0.79	69.0 ± 1.35
DirGNN/TFE (baseline) (Rossi et al., 2024)	84.6±0.61	71.5±0.88	59.8 ± 1.45	35.2±1.13	27.5±0.95	68.8±1.57
DirGNN/TFE + SignGate (ours)	$84.8 {\pm} 0.58$	72.0 ± 0.80	61.2 ± 1.34	36.1 ± 0.95	$28.3 {\pm} 0.81$	71.1 ± 1.50
GESC w/ scalar gate	84.0 ± 0.62	71.1 ± 0.66	63.1 ± 1.30	36.8 ± 0.88	29.0 ± 0.77	72.4 ± 1.44

D.6. Isolating Novelty via Cross-Substitution

To rigorously verify the origin of GESC's improvement, we perform cross-substitution experiments where its core modules are interchanged with those from strong baselines under matched parameters and compute budgets. Specifically, we inject the Self-Interference Cancellation (SIC) into MSGNN, apply the Gauge-Equivariant Transport (GET) mechanism to MagNet, and substitute the Sign-Aware Gating in place of the spectral reweighting used in DirGNN and TFE. Conversely, we ablate GESC by replacing each corresponding module with the baseline's component. Table 7 presents the results across six representative benchmarks. Injecting SIC into MSGNN yields consistent gains of +0.5-1.6%, confirming that suppressing self-aligned redundant signals enhances discriminability under heterophily. Similarly, integrating GET into MagNet improves robustness by up to +2.7% on high-frequency datasets (Chameleon and Squirrel), demonstrating that gauge-consistent phase transport mitigates local orientation noise. Replacing DirGNN/TFE's spectral weighting with our sign-aware gating also produces small yet stable improvements, highlighting the benefit of adaptive polarity control in mixed-homophily settings. In contrast, when the same modules are swapped out from GESC and replaced with baseline mechanisms, performance consistently declines by 1-2%. These symmetric trends clearly isolate SIC, Sign-Aware Gating, and GET as the principal contributors to GESC's overall superiority, providing concrete empirical evidence that its advantage arises from genuinely novel components rather than cumulative tuning effects.